

# *XMM-Newton* observations of the Lockman Hole IV: spectra of the brightest AGN <sup>★</sup>

S. Mateos<sup>1,2</sup>, X. Barcons<sup>1</sup>, F. J. Carrera<sup>1</sup>, M. T. Ceballos<sup>1</sup>, G. Hasinger<sup>3</sup>, I. Lehmann<sup>3</sup>, A. C. Fabian<sup>4</sup>, and A. Streblyanska<sup>3</sup>

<sup>1</sup> Instituto de Física de Cantabria (CSIC-UC), 39005 Santander, Spain

<sup>2</sup> X-ray Astronomy Group, Department of Physics and Astronomy, Leicester University, Leicester LE1 7RH, UK

<sup>3</sup> Max-Planck-Institut für Extraterrestrische Physik, Giessenbachstrasse, Garching D-85748, Germany.

<sup>4</sup> Institute of Astronomy, University of Cambridge, Madingley Road, Cambridge CB3 0HA, UK.

29 June 2005

**Abstract.** This paper presents the results of a detailed X-ray spectral analysis of a sample of 123 X-ray sources detected with *XMM-Newton* in the *Lockman Hole* field. This is the deepest observation carried out with *XMM-Newton* with more than 600 ksec of good EPIC-pn data. We have spectra with good signal to noise ( $>500$  source counts) for all objects down to 0.2-12 keV fluxes of  $\sim 5 \times 10^{-15}$  erg cm<sup>-2</sup> s<sup>-1</sup> (flux limit of  $\sim 6 \times 10^{-16}$  erg cm<sup>-2</sup> s<sup>-1</sup> in the 0.5-2 and 2-10 keV bands). At the time of the analysis, we had optical spectroscopic identifications for 60% of the sources, 46 being optical type-1 AGN and 28 optical type-2 AGN. Using a single power law model our sources' average spectral slope hardens at faint 0.5-2 keV fluxes but not at faint 2-10 keV fluxes. We have been able to explain this effect in terms of an increase in X-ray absorption at faint fluxes. We did not find in our data any evidence for the existence of a population of faint intrinsically harder sources. The average spectral slope of our sources is  $\sim 1.9$ , with an intrinsic dispersion of  $\sim 0.28$ . We detected X-ray absorption (F-test significance  $\geq 95\%$ ) in 37% of the sources,  $\sim 10\%$  in type-1 AGN (rest-frame  $N_{\text{H}} \sim 1.6 \times 10^{21} - 1.2 \times 10^{22}$  cm<sup>-2</sup>) and  $\sim 77\%$  (rest-frame  $N_{\text{H}} \sim 1.5 \times 10^{21} - 4 \times 10^{23}$  cm<sup>-2</sup>) in type-2 AGN. Using X-ray fluxes corrected for absorption, the fraction of absorbed objects and the absorbing column density distribution did not vary with X-ray flux. Our type-1 and type-2 AGN do not appear to have different continuum shapes, but the distribution of intrinsic (rest-frame) absorbing column densities is different among both classes. A significant fraction of our type-2 AGN (5 out of 28) were found to display no substantial absorption ( $N_{\text{H}} < 10^{21}$  cm<sup>-2</sup>). We discuss possible interpretations to this in terms of Compton-thick AGN and intrinsic Broad Line Region properties. An emission line compatible with Fe K $\alpha$  was detected in 8 sources (1 type-1 AGN, 5 type-2 AGN and 2 unidentified) with rest frame equivalent widths 120-1000 eV. However weak broad components can be easily missed in other sources by the relatively noisy data. The AGN continuum or intrinsic absorption did not depend on X-ray luminosity and/or redshift. Soft excess emission was detected in 18 objects, but only in 9 (including 4 type-1 AGN and 4 type-2 AGN) could we fit this spectral component with a black body model. The measured 0.5-2 keV luminosities of the fitted black body were not significantly different in type-1 and type-2 AGN, although the temperatures of the black body were slightly higher in type-2 AGN ( $\langle kT \rangle = 0.26 \pm 0.08$ ) than in type-1 AGN ( $\langle kT \rangle = 0.09 \pm 0.01$ ). For 9 sources (including 1 type-1 AGN and 3 type-2 AGN) a scattering model provided a better fit of the soft excess emission. We found that the integrated contribution from our sources to the X-ray background in the 2-7 keV band is softer ( $\Gamma = 1.5 - 1.6$ ) than the background itself, implying that fainter sources need to be more absorbed.

**Key words.** X-rays: general, X-rays: diffuse background, surveys, galaxies: active

## 1. Introduction

The extragalactic X-ray background (XRB) at energies above  $\sim 0.2$  keV is made up of the integrated emission from point sources, mostly Active Galactic Nuclei (AGN). Synthesis models of the XRB (e.g. Setti & Woltjer, 1989; Gilli et al., 2001; Ueda et al., 2003), based on unification schemes of AGN, can

reproduce the spectral shape of the XRB with the superposition of a mixture of absorbed and unabsorbed AGN. There is much observational evidence supporting the unified model of AGN (Antonucci, 1993). For example the discovery of large columns of X-ray absorbing gas in type-2 AGN (Awaki et al., 1991; Risaliti et al., 1999), and the lack of this absorbing material in type-1 AGN.

Send offprint requests to: S. Mateos, e-mail: sm279@star.le.ac.uk

<sup>★</sup> Based on observations obtained with *XMM-Newton*, an ESA science mission with instruments and contributions directly funded by ESA Member States and NASA

With the launch of the *Chandra* and *XMM-Newton* observatories, our knowledge of the nature and cosmic evolution of AGN has increased significantly. However the amount of ob-

arXiv:astro-ph/0506718v1 29 Jun 2005

servational results that cannot be explained in terms of the unified model of AGN is also significant. There is a substantial number of type-1 AGN for which X-ray absorption has been detected (Mittaz et al., 1999; Fiore et al., 2001; Page et al., 2001; Schartel et al., 2001; Tozzi et al., 2001; Mainieri et al., 2002; Brusa et al., 2003; Page et al., 2003; Carrera et al., 2004; Perola et al., 2004; Mateos et al., 2005), as well as Seyfert 2 galaxies unabsorbed in X-rays (Pappa et al., 2001; Panessa et al., 2002; Barcons et al., 2003; Mateos et al., 2005). The origin of the X-ray absorption in type-1 AGN is still not clear. Possible explanations include cold gas in the host galaxy.

For all these objects their optical and X-ray properties cannot be explained in terms of an orientation effect only.

In order to gain insight into these problems and to understand better the X-ray emission and cosmic evolution of the AGN that make up most of the XRB, spectral analysis of large samples of AGN detected in medium and deep X-ray surveys have been or are being conducted (Mainieri et al., 2002; Piconcelli et al., 2002, 2003; Georgantopoulos et al., 2004; Caccianiga et al., 2004; Perola et al., 2004; Della Ceca et al., 2004; Mateos et al., 2005). However, at the moment, only a small number of these studies have carried out a proper spectral analysis of the spectra of each individual source, and in many cases some assumptions had to be made prior to the spectral analysis (frequently on the spectral slope). These studies provide observational constraints with large uncertainties.

The *Lockman Hole* field is one of the sky regions best studied at X-ray wavelengths, because the Galactic absorbing column density in this direction is minimal ( $5.7 \times 10^{19} \text{cm}^{-2}$ , see Lockman et al., 1986).

*XMM-Newton* has carried out its deepest observation in the direction of the *Lockman Hole* field. These observations have allowed us to extract good quality ( $>500$  0.2–12 keV counts) X-ray spectra for objects down to 0.2–12 keV fluxes of  $\sim 5 \times 10^{-15} \text{erg cm}^{-2} \text{sec}^{-1}$  (the flux limit is  $\sim 6 \times 10^{-16} \text{erg cm}^{-2} \text{sec}^{-1}$  in the 0.5–2 and 2–10 keV energy bands). We have used the *XMM-Newton* observations in the *Lockman Hole* to carry out a detailed analysis of the X-ray emission of the 123 brightest objects detected in the field. The results from the analysis of a sample of fainter objects will be described in a forthcoming paper.

Using a subset of these observations, Hasinger et al. (2001) presented the source detection and properties of X-ray sources. Mainieri et al. (2002) conducted a X-ray spectral analysis of the objects detected in the field. Worsley et al. (2004, 2005) used the total observation of the field to calculate the fraction of unresolved XRB in different energy bands. Finally Streblyanska et al. (2005) have conducted a detailed study of the Fe K $\alpha$  emission in the stacked spectra of type-1 and type-2 AGN. They found in their analysis indications for broad relativistic lines in both type-1 and type-2 AGN.

This paper is organised as follows: Sec. 2 describes the X-ray data that we used for the analysis; Sec. 3 describes how we built our sample of objects; Sec. 4 explains how the time averaged spectra were extracted for each individual object; in Sec. 5 we show the current status of the optical identification process; Sec. 6 describes the models that we used to fit the X-ray emission of our sources; we show the results of the analysis

in Sec. 7, Sec. 8 and Sec. 9; the dependence of spectral parameters with luminosity and redshift is shown in Sec. 10; In Sec. 11 we discuss possible explanations for the lack of X-ray absorption signatures found in the spectra of five of the sources in our sample of type-2 AGN; In Sec. 12 we compare the integrated emission of our sources with the cosmic X-ray background in the 2–7 keV band; the results of our analysis are summarised in Sec. 13.

Throughout this paper we have adopted the *WMAP* derived cosmology with  $H_0 = 70 \text{ km s}^{-1} \text{ Mpc}^{-1}$ ,  $\Omega_M = 0.3$  and  $\Omega_\Lambda = 0.7$ . All errors are computed with a delta chi-square of 2.706, equivalent to 90% confidence region for a single parameter.

## 2. *XMM-Newton* observations

The deepest *XMM-Newton* observation has been carried out in the direction of the *Lockman Hole* field, that is centred on the sky position RA: 10:52:43 and DEC: +57:28:48 (J2000). The data were obtained by adding 17 *XMM-Newton* observations obtained from 2000 to 2002. A summary of the observations used in this analysis is given in Table 1. The *Lockman Hole* was also observed during revolution 071, however at the time of this analysis there was no Observation Data File (ODF) available, and hence, we could not reprocess the data. The first column in Table 1 shows the revolution number and observation identifier. The second column shows the phase of the observation (i.e. PV for observations during the EPIC-Payload Verification Phase, and AO1 and AO2 for observations during the first and second Announcement of Opportunity). The third and fourth columns list the coordinates of the field used for each observation. The next column lists the observation dates and the last three columns show the filters that were used during each observation for each X-ray detector together with the exposure times after removal of periods of high background. The 17 *XMM-Newton* observations gave a total exposure (after removal of periods of high background) of  $\sim 850$  ksec for MOS1 and MOS2 detectors and  $\sim 650$  ksec for pn. Some AO2 observations have an offset of more than  $\sim 25$  arcmin with respect to the other observations. Because of this offset between observations, the total exposure time in the centre of the *Lockman Hole* field was reduced significantly, however, the total solid angle covered by the observations increased substantially. The solid angle of the observation as a function of the effective exposure time<sup>1</sup> is plotted in Fig. 1.

## 3. X-ray source list

We have used the *XMM-Newton* Science Analysis Software (SAS, Gabriel et al. 2004) version v5.4, the latest public version of the SAS at the time of study, to analyse the X-ray observations. Spurious noise events not created by X-rays were filtered from the event files using the *XMM-Newton* pipeline

<sup>1</sup> The solid angle for a value of  $t$  was obtained by summing the number of pixels in M1, M2 and pn exposure maps of the total observation with a value  $\geq t$ . Because the exposure maps include the energy dependent mirror vignetting function, the solid angle is given as a function of the effective exposure time on each camera

**Table 1.** Summary of *XMM-Newton* observations in the *Lockman Hole*

rev/obs. id	obs phase	RA	DEC	obs. date	Filter <sup>a</sup> /GTI <sup>b</sup>		
		(J2000)	(J2000)		EPIC-pn	EPIC-MOS1	EPIC-MOS2
070/0123700101	PV	10 52 43.0	+57 28 48	2000-04-27	Th/34	Th/34	Tck/33
073/0123700401	PV	10 52 43.0	+57 28 48	2000-05-02	Th/14	Th/14	Tck/14
074/0123700901	PV	10 52 41.8	+57 28 59	2000-05-05	Th/5	Th/8	Tck/5
081/0123701001	PV	10 52 41.8	+57 28 59	2000-05-19	Th/27	Th/36	Tck/28
345/0022740201	AO1	10 52 43.0	+57 28 48	2001-10-27	M/40	M/37	M/24
349/0022740301	AO1	10 52 43.0	+57 28 48	2001-11-04	M/35	M/34	M/31
522/0147510101	AO2	10 51 03.4	+57 27 50	2002-10-15	M/79	M/81	M/55
523/0147510801	AO2	10 51 27.7	+57 28 07	2002-10-17	M/55	M/56	M/46
524/0147510901	AO2	10 52 43.0	+57 28 48	2002-10-19	M/55	M/57	M/50
525/0147511001	AO2	10 52 08.1	+57 28 29	2002-10-21	M/78	M/79	M/61
526/0147511101	AO2	10 53 17.9	+57 29 07	2002-10-23	M/45	M/52	M/27
527/0147511201	AO2	10 53 58.3	+57 29 29	2002-10-25	M/30	M/34	M/23
528/0147511301	AO2	10 54 29.5	+57 29 46	2002-10-27	M/28	M/33	M/14
544/0147511601	AO2	10 52 43.0	+57 28 48	2002-11-27	M/104	M/103	M/68
547/0147511701	AO2	10 52 40.6	+57 28 29	2002-12-04	M/98	M/98	M/89
548/0147511801	AO2	10 52 45.3	+57 29 07	2002-12-06	M/86	M/86	M/72

<sup>a</sup> Blocking filter: Th: Thin at 40nm Al; M: Medium at 80nm Al; Tck: Thick at 200nm Al

<sup>b</sup> Exposure time (in ksec) per observation and detector obtained after removal of background flares

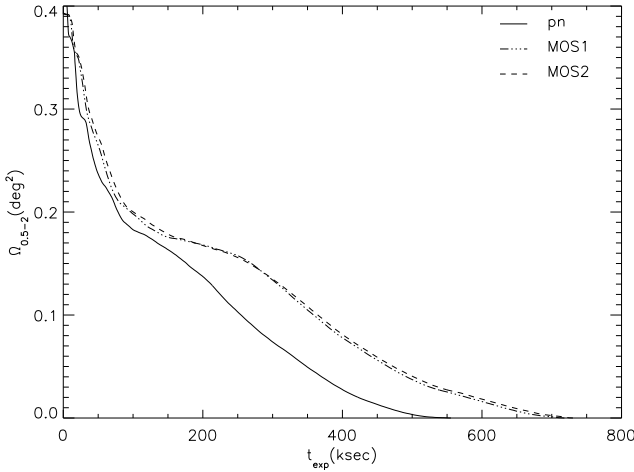


**Fig. 1.** Solid angle( $\Omega(t)$ ) covered by MOS1, MOS2 and pn detectors as a function of the effective exposure time (after removal of background flares) in the 0.5-2 keV band.  $\Omega(t)$  is the solid angle (in  $\text{deg}^2$ ) in the 0.5-2 keV exposure map of each EPIC camera with an exposure  $\geq t$ .

standard filtering. We have cleaned the event files of the individual observations with periods of high background due to soft high background flares. For each observation and detector we

built light curves (histograms of counts as a function of time). The light curves were visually inspected to search for time intervals affected by high flaring background periods. Thresholds in count rate were determined separately for each observation and camera.

Events covering patterns 0-12 for MOS and 0-4 for pn data were selected.

Cleaned event files were used to create images, background maps and exposure maps for each detector and for each of the *XMM-Newton* standard energy bands (0.2-0.5, 0.5-2, 2-4.5, 4.5-7.5 and 7.5-12 keV). We have run the *XMM-Newton* source detection algorithm, `eboxdetect-emldetect`, simultaneously in the five energy bands. Our motivation was to reach the maximum sensitivity in each individual band in order to best detect objects with spectra peaking at different energies (as it is the case for AGN with different absorbing column densities). However, it is important to note that the sensitivity of the *XMM-Newton* X-ray detectors is a strong function of energy, with the maximum sensitivity reached between 0.5 and 4.5 keV. This implies that we will best detect objects with X-ray spectra peaking within this interval of energy.

Due to the large offset between different observations of the field (see Sec. 2), we did not merge the event files, because in the merging process important information from the individual observations is lost (e.g., bad columns in the detectors). Moreover, it is not possible to create exposure maps or back-

ground maps from the merged event files. Therefore we extracted images, exposure maps and background maps, for each individual observation, detector and energy band, and then, we combined them to obtain the total observation of the field for each X-ray detector and energy band.

We decided to run the source detection algorithm independently for each detector. Because the pn data give the deepest observation of the field (the MOS1 and MOS2 detectors only receive about half of the radiation from the X-ray telescopes, the other half goes to the Reflection Grating Spectrometers), we used the pn source list to build our catalogue of sources. However, we cross-correlated the sources detected with the pn with the ones detected with each MOS detector. We found that only one faint object that was detected with the MOS1 and MOS2 detectors was not detected with the pn (probably because it was very close to a brighter object). We added this object to our source list. We have carried out a visual screening of the objects to remove spurious detections (e.g. we have detections in hot pixels that were still present in the data). The final number of objects detected after visual screening in the integrated *XMM-Newton* observation of the *Lockman Hole* is 268.

In this paper we show the results obtained from the spectral analysis of the 123 sources with the best spectral quality (more than 500 MOS+pn background subtracted counts in the 0.2-12 keV band). Because we were interested in studying the X-ray spectral properties of AGN, we excluded from the sample the objects identified as clusters of galaxies or stars. The results from the analysis of the fainter objects will be presented in a forthcoming paper. Fig. 2 shows the distribution of (background subtracted) counts for the sources that we have studied. In the following we will refer to the sample of 123 brightest sources as our list of objects.

In order to allow comparison with previous surveys conducted in the soft, 0.5-2 keV, and hard, 2-10 keV, bands, we have checked whether our objects were detected in any of these bands. We have the likelihoods of detection for the soft band, because it was one of the energy bands used for the source detection. We have calculated the likelihoods in the hard (2-10 keV) band, combining<sup>2</sup> the ones obtained in the bands 2-4.5 keV, 4.5-7.5 keV and 7.5-12 keV. Indeed, the combination of these values will give us the detection likelihood in band 2-12 keV. However, the effective area of the X-ray telescopes decreases rapidly at energies above 5 keV, hence we do not expect the value of the detection likelihood in the 2-12 keV band to differ substantially from the value in the 2-10 keV band. By selecting sources with 0.5-2 and 2-10 keV detection likelihoods above 10 we found that the number of objects detected in both the soft and hard bands was 117 (out of 123). Three objects were only detected in the hard band and three only in the soft band. These numbers indicate that the source population that we are studying is detected in both bands, and therefore our list of sources does not differ significantly from what would have been detected in a hard or soft band survey at similar fluxes.

<sup>2</sup> Detection likelihoods in the 2-10 keV band were obtained following the description of the `emldetect` task, see [http://xmm.vilspa.esa.es/external/xmm\\_sw\\_cal/sas\\_frame.shtml](http://xmm.vilspa.esa.es/external/xmm_sw_cal/sas_frame.shtml)

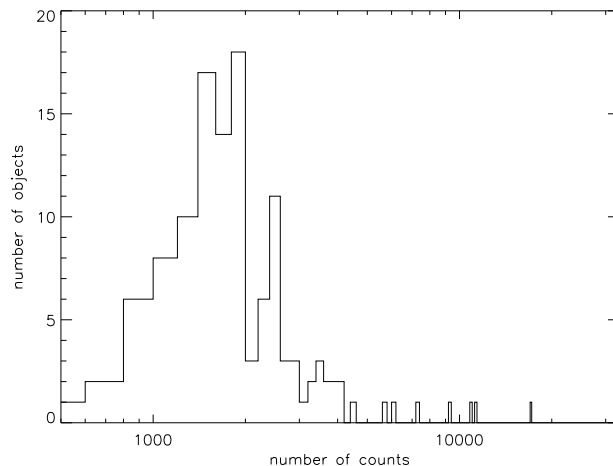


**Fig. 2.** Distribution of the number of background-subtracted counts in the 0.2-12 keV spectra for the sources in our sample. We used the counts of the time averaged spectra with better signal to noise (MOS or pn)

#### 4. X-ray spectral products

An automated procedure has been used to obtain for each individual object the spectrum of the total observation, hereafter, the time averaged spectrum of the sources. In addition a background spectrum and a response calibration matrix have been generated by combining individual products from each exposure.

First we have extracted the spectra of each object for each detector (MOS1, MOS2 and pn) and observation. We used the coordinates of the objects, RA and Dec, that we obtained from the source detection process, and the SAS task `region` to define the source and background extraction regions. The first was defined as a circle with a radius ( $r_s$ ) that varied depending on the position of the source within the detector. We extracted the background for each object in an annulus centred on the source position, with inner radius  $r_s$  and outer radius  $3 \times r_s$ . The task `region` checks the source and background regions for overlap with neighbouring sources. If overlapping exists, then, the size of the source region is reduced until it is removed. For the background regions, if neighbouring objects fall inside the background region they are masked out. The task `region` also checks that the extraction regions do not extend outside the edges of the field of view. The radius of extraction of spectra varies from source to source, but typically was  $\sim 14$ -20 arcsec. Once the regions were defined, we used the SAS task `evselect` to extract from event files the spectra of each object. Calibration matrices (`arf` and `rmf`) for each spectrum were obtained with the SAS tasks `arfgen` and `rmfgen`.

We did not use the spectra from observations where the objects were near the borders of the FOV, or near CCD gaps or bad columns, because in these cases we found that the spectral products, in particular the response matrices were often incorrect. To find and remove these cases we visually checked the images of each observation and detector.

We have obtained a MOS and pn time averaged spectra for each object. As we see in Table 1, different filters were used for the observations. The filters affect in a different way the X-ray spectra at low energies. To take into account this effect when combining the spectral products of each source, we have weighted the data of each individual observation with the exposure time of the observation.<sup>3</sup>

The spectra were extracted in the energy range from 0.2 to 12 keV, where the X-ray detectors are best calibrated. In order to use the  $\chi^2$  minimisation during the spectral fitting, we have grouped the spectra with a minimum number of 30 counts per bin.

## 5. Optical identifications

A large fraction of the X-ray sources that were detected with the *ROSAT* satellite in the *Lockman Hole* have already been identified through optical spectroscopy (Schmidt et al., 1998; Lehmann et al., 2001). These sources were detected in the 0.5–2 keV energy range, and therefore the optical identification is expected to be biased against absorbed sources, whose X-ray spectra does not peak in the *ROSAT* energy interval. However, the optical identifications go as deep as  $R \sim 24$ , hence we do not expect the identifications in our sample to be significantly affected by the bias against absorbed sources.

Our *XMM-Newton* observations cover a larger solid angle than the *ROSAT* observations and find additional sources due to the superb high energy response of the *XMM-Newton* detectors. Some of the objects that we have analysed fall outside the solid angle covered by *ROSAT* and we do not have optical identifications. Other sources were not detected with *ROSAT*. For 8 of these newly detected *XMM-Newton* sources optical spectra have been obtained with the LRIS and Deimos instruments at the Keck telescopes in 2001, 2003, and 2004 (PI: M. Schmidt and P. Henry). The spectroscopic identification of these objects and of the entire Deep *XMM-Newton* Survey in the *Lockman Hole* will be presented in a forthcoming paper (Lehmann et al. 2005 in preparation).

To be consistent with the *ROSAT* identifications we have used the same criteria to differentiate between type-1 and type-2 AGN as described in detail by Schmidt et al. (1998). Sources were classified depending on the properties of their UV/optical emission lines. Objects with UV/optical emission lines with  $FWHM > 1500 \text{ km s}^{-1}$  in their optical spectra were classified as type-1 AGN. Sources that do not exhibit broad emission lines but that show Ne emission lines ([Ne V] and/or strong [Ne III]) were classified as type-2 AGN. Classification of Narrow Line Seyfert 1 galaxies (NLSy1) was only possible for bright nearby objects. Hence, we cannot be sure that the optical classification criteria used to separate the type-1 and type-2 AGN in our sample has excluded all NLSy1 from the sample of type-2 AGN. However, based on the observed X-ray properties of our sources, we do not expect this to affect the results of our study.

<sup>3</sup> Source and background spectra are obtained adding the counts for each channel. The areas used to extract the spectra and the response

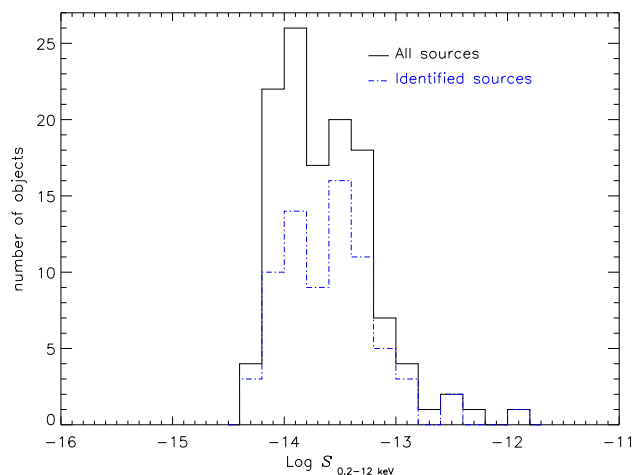


**Fig. 3.** Histograms of 0.2–12 keV fluxes for the whole sample of sources analysed and for the objects with optical identifications. The fluxes were obtained from the sources best fit model (See Sec. 9).

At the time of this analysis, 74 ( $\sim 60\%$ ) of the sources had optical spectroscopic identifications. Of these, 46 were classified as type-1 AGN and 28 as type-2 AGN.

In Fig. 3 we show the distribution in 0.2–12 keV flux<sup>4</sup> of all the objects (solid histogram) and of the identified sources (dashed histogram). We see that the two distributions agree quite well, i.e., the identified sources do not tend to have higher X-ray fluxes.

## 6. X-ray spectral fitting

We have used the *xspec* 11.3.0 package to fit the X-ray spectra of our objects. MOS and pn spectra were fitted simultaneously and with the same spectral model, including normalisation. At the time of our analysis it was found that there was an offset of  $\sim 1$  arcmin between the optical axis of the three EPIC instruments and the values in the calibration files (CCF)<sup>5</sup>. This could be introducing discrepancies in the fluxes measured by the MOS and pn due to an incorrect vignetting correction. These flux discrepancies could be as high as  $\pm 14\%$ . However, we did not find a significant improvement in the quality of our fits when different normalisations were used to fit MOS and pn spectra. For the objects where we found an offset between MOS and pn normalisations, this offset was much higher than the expected flux discrepancies explained before. We interpreted this effect as a change in the flux of the source during the observations (note that the time averaged spectra of MOS and pn in the majority of the cases were not necessary built with the same set of observations, because the FOV and the positions of the gaps are different for MOS and pn, and in different observations).

matrices were weighted with the exposure times of each individual observation.

<sup>4</sup> Fluxes were obtained from the objects best fit model (See Sec. 9)

<sup>5</sup> <http://xmm.vilspa.esa.es/docs/documents/CAL-SRN-0156-1-3.ps.gz>

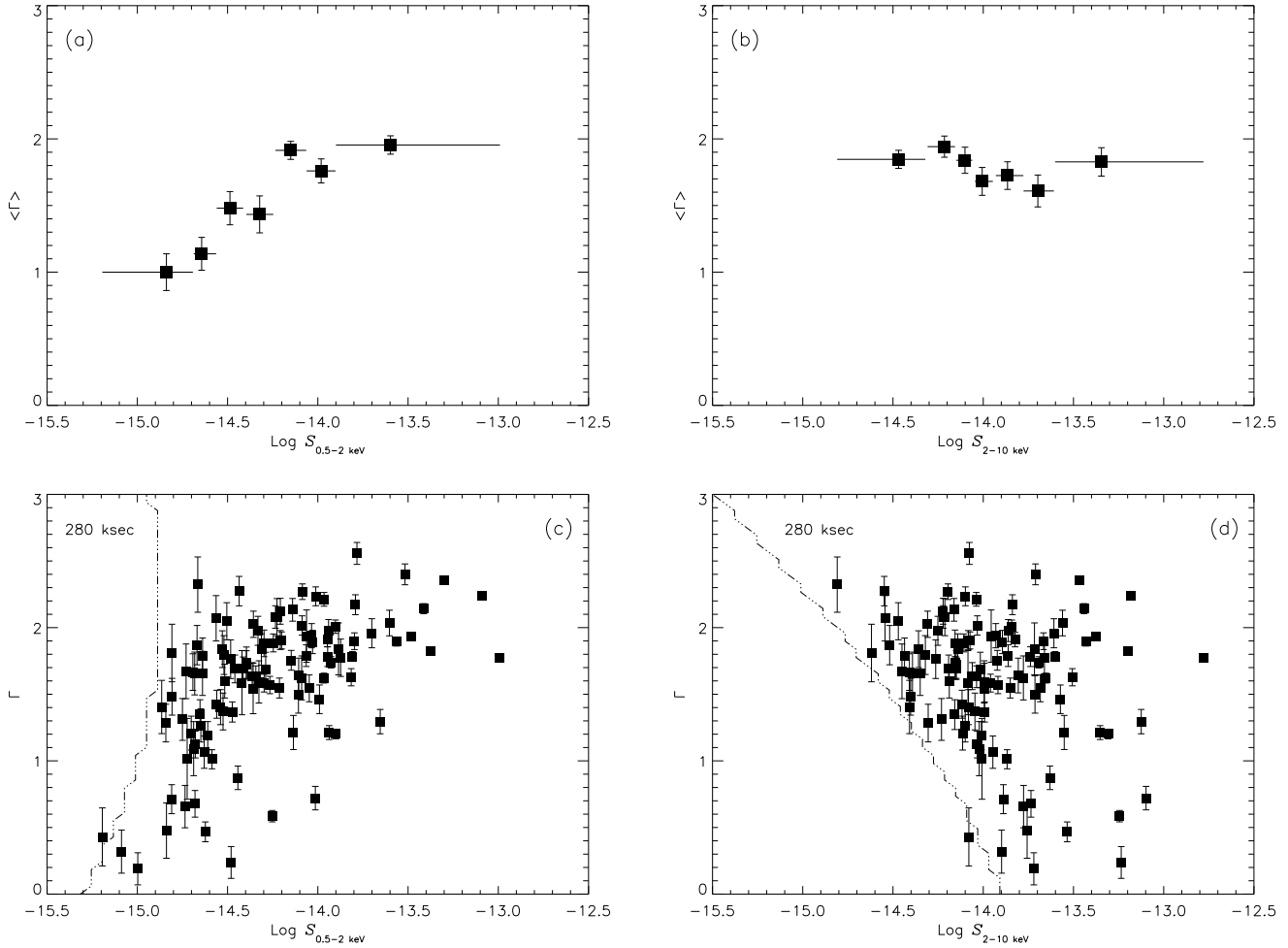


**Fig. 4.** Dependence of  $\Gamma$  with soft (0.5-2 keV) and hard (2-10 keV) flux when all spectra are fitted with a single power law model. In plots (a) and (b) we show the dependence of the weighted (with the error of each individual value)  $\Gamma$  with the flux. The bins in flux were defined in order to have the same number of sources per bin. In plots (c) and (d) we show the values of  $\Gamma$  obtained for each individual source. The dash-dot lines in these plots show, for an exposure time of 280 ksec, the limit in flux for detection for an object as a function of  $\Gamma$  (see Sec. 7.1 for details). Errors bars in (c) and (d) correspond to 90% confidence.

In order to compare the results of our analysis with other studies of data with lower signal to noise, we have fitted the spectra of our sources with a single power law model (hereafter SPL). This has allowed us to study in more detail the origin of the hardening of the average spectra of AGN with the soft X-ray flux (see e.g. Mateos et al 2005), and investigate if the same effect is also present when 2-10 keV fluxes are used. To study the effect of absorption in the results obtained with the SPL we fitted all the spectra with an absorbed power law model (hereafter APL model).

Using these two models it is possible to obtain very useful results on the average spectral properties of our sources, the broad band continuum shape and the X-ray absorption. However, our major goal is to study in detail the 0.2-12 keV X-ray emission of each individual source. Hence, for each object we have obtained its best fit model. The quality of our data has allowed us to search for soft excess at low energies, the Fe  $K\alpha$  emission line complex, and reflection components.

We have used the F-test to measure the significance of detection for each spectral component. We have selected a confidence level threshold of 95% to accept an additional spectral component as being real. The criteria that we used to select X-ray absorbed sources is to have an F-test significance  $\geq 95\%$ . This is different from some definitions found in the literature, because we did not impose a lower threshold in the detected values of  $N_{\text{H}}$ . For example, Ueda et al. (2003) defined as X-ray absorbed the sources with absorption column density at the source redshift  $\geq 10^{22} \text{ cm}^{-2}$ . However, it is important to note that with our criteria all sources selected as X-ray absorbed had values of  $N_{\text{H}} \geq 21 \text{ cm}^{-2}$ .

## 7. Single power law fitting (SPL)

We have used a single power law model to fit the 0.2-12 keV emission of all the objects. In this model, the free parameters are the normalisation (the same for MOS and pn spectra) and

the slope of the broad band continuum,  $\Gamma$ <sup>6</sup>. The power law is absorbed with a fixed column density of  $5.7 \times 10^{19} \text{ cm}^{-2}$  to include the effect of the absorption by our Galaxy in the direction of the *Lockman Hole* field.

### 7.1. Dependence of $\Gamma$ with the X-ray flux

The results of the fits have been used to study the dependence of  $\Gamma$  with the X-ray fluxes obtained from the SPL model. The results are plotted in Fig. 4. In plots (a) and (b) we show the dependence of  $\langle\Gamma\rangle$  with the 0.5-2 keV and 2-10 keV fluxes. The bin sizes were defined in order to have the same number of objects per bin, and the average values were obtained weighting with the errors of each individual value. When a single power law model is used, we see that the average continuum shape becomes harder with decreasing 0.5-2 keV flux. However, it is interesting to note that we do not see any dependence of  $\langle\Gamma\rangle$  with the 2-10 keV flux down to  $\sim 3 \times 10^{-15} \text{ erg cm}^{-2} \text{ s}^{-1}$ .

The values of  $\langle\Gamma\rangle$  were calculated with the standard formula for the weighted mean,

$$\langle\Gamma\rangle = \sum P_i \times \Gamma_i$$

where the weight,  $P_i$ , of each individual best fit value,  $\Gamma_i$ , is a function of the error in the parameter obtained from the fit,  $\sigma_i$ , i.e.

$$P_i = \frac{1/\sigma_i^2}{\sum (1/\sigma_i^2)}$$

To calculate the uncertainty in  $\langle\Gamma\rangle$  we have used the error on the weighted mean (Bevington et al. 1992),

$$\sigma^2(\langle\Gamma\rangle) = \frac{1}{(N-1)} \sum P_i \times (\Gamma_i - \langle\Gamma\rangle)^2$$

that includes the measurement errors,  $\sigma_i$ , and the dispersion of each  $\Gamma_i$  from the estimated value  $\langle\Gamma\rangle$ . Using these expressions we found that our objects have  $\langle\Gamma\rangle = 1.79 \pm 0.03$  when their spectra are fitted with a SPL (the value is  $1.60 \pm 0.05$  if we use the unweighted mean).

In order to understand better the origin of the hardening of  $\langle\Gamma\rangle$  with the 0.5-2 keV flux, and why we do not see the same effect using 2-10 keV fluxes, we have plotted in Fig. 4 (figures (c) and (d)) the values of  $\Gamma$  that we obtained for each individual object. Thanks to the good quality of our data we can see that  $\langle\Gamma\rangle$  becomes harder because at faint 0.5-2 keV fluxes a population of faint sources is revealed with very hard ( $\leq 1$ ) spectral slopes. We also see that the number of faint hard objects becomes more important as we go to fainter fluxes. In the 2-10 keV band we do not see the hardening of  $\langle\Gamma\rangle$  because these hard objects are detected at all 2-10 keV fluxes. Moreover, their number seems not to vary with the 2-10 keV flux.

We have studied whether our criteria for selection of objects (i.e. MOS+pn background subtracted counts above 500) could be introducing any bias in our results. In particular we have studied whether, for a given flux, we are favouring objects with a given spectral slope. To study this, we have carried

out simulations. We first defined a grid of points in  $\Gamma$  and  $S$  (first using 0.5-2 keV flux and later with 2-10 keV flux), covering the same range of  $\Gamma$ - $S$  values as our sources. Using a pair of on-axis response matrices, *arf* and *rmf*, and typical background spectra selected from one of our objects, we have simulated a spectrum on each grid point. With the simulated spectra we have calculated the minimum exposure time that is needed to reach the threshold in number of counts that we have used to select our sources (i.e. 500 MOS+pn background subtracted counts). With these simulations we were not interested in quantifying the limits of detection as a function of  $S$  and  $\Gamma$ , but to study the biases in our sample, and whether they affect our results. Therefore we only need to do one simulation on each grid point and then we just have to search for the points in the  $\Gamma$ - $S$  grid with the same value of the exposure time.

A constant exposure time line to get 500 counts is represented with the dot-dash lines in plots (c) and (d) on Fig. 4 for an exposure time of 280 ksec. We see that in the soft band, for a given flux, we have the same efficiency of detection for different values of  $\Gamma$  down to 1.5. At fluxes above  $\sim 10^{-15} \text{ erg cm}^{-2} \text{ s}^{-1}$  this bias is not affecting the observed hardening of  $\Gamma$ . Only the bin at the faintest 0.5-2 keV fluxes (plot (a)) could be affected by this bias. Our simulations show that the hardening in  $\langle\Gamma\rangle$  is an intrinsic property of our objects. As we said in Sec. 3, our objects were all detected in the soft band, therefore this effect is a property of the 0.5-2 keV population of objects. The objects responsible for the hardening of  $\langle\Gamma\rangle$  can be more absorbed sources or sources having intrinsically harder spectra.

In the 2-10 keV band we obtained different results from the simulations. At the faintest fluxes we most easily detect objects with soft spectra. This is an expected result because the effective area of the X-ray detectors in *XMM-Newton* decreases rapidly at energies  $\geq 5$  keV and therefore it is more difficult to detect faint objects with flat spectral slopes. However, down to the flux level where we start to lose faint hard objects,  $\sim 6 \times 10^{-15} \text{ erg cm}^{-2} \text{ s}^{-1}$ , we see that there is no dependence of  $\Gamma$  with hard flux because hard objects are detected at all flux levels.

## 8. Absorbed power law fitting (APL)

In order to study the nature of the population of faint hard sources responsible for the hardening of  $\langle\Gamma\rangle$  with the 0.5-2 keV flux we have fitted the spectra of all the objects with an absorbed power law model. The free parameters of this model are the normalisation, the spectral slope of the power law component, and the intrinsic (rest-frame) absorption of the objects that we have measured in the observer's frame ( $N_{\text{H}}^{\text{obs}}$ ). Again, we also included the effect of the Galactic absorption in the direction of the *Lockman Hole*. Using the APL model we obtained a value for the weighted mean of  $\langle\Gamma\rangle = 1.87 \pm 0.04$  (the value being  $\langle\Gamma\rangle = 1.95 \pm 0.08$  using the arithmetic mean) for the objects where absorption was detected (F-test  $\geq 95\%$ ), and  $\langle\Gamma\rangle = 1.95 \pm 0.03$  (the value being  $\langle\Gamma\rangle = 1.82 \pm 0.04$  using the arithmetic mean) for the objects where we did not detect absorption (F-test  $< 95\%$ ).

<sup>6</sup> We use the power law photon number index,  $\Gamma$ . Its relation with the energy index is  $\alpha = \Gamma - 1$

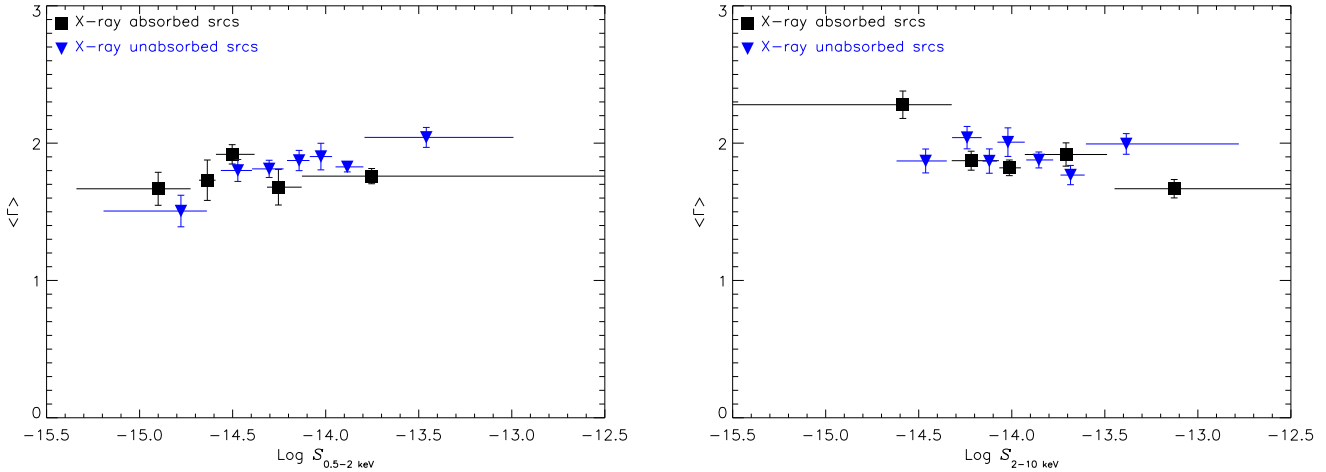


**Fig. 5.** Dependence of  $\langle \Gamma \rangle$  with 0.5-2 and 2-10 keV flux for absorbed (F-test  $\geq 95\%$ ) and unabsorbed (F-test  $< 95\%$ ) sources. For each source we used  $\Gamma$  and  $S$  from its best fit model (single power law or absorbed power law). See Sec. 8 for details.

The dependence of  $\langle \Gamma \rangle$  on 0.5-2 keV and 2-10 keV fluxes that we see fitting the spectra of our objects with the APL model is shown in Fig. 5. For the objects where absorption was detected we used the spectral parameters ( $\Gamma$  and observed  $S$ ) obtained with the APL model. For the unabsorbed sources we used the parameters from the SPL model. We see that absorption can account for most of the hardening of  $\langle \Gamma \rangle$  with the soft X-ray flux. We also see in Fig. 5 that the same dependence of  $\langle \Gamma \rangle$  with the X-ray flux is obtained for absorbed and unabsorbed objects.

Mateos et al. (2005) found that for their serendipitous X-ray sources (with much lower spectral quality), the average spectrum of unabsorbed (F-test significance  $< 95\%$ ) sources significantly hardens at faint 0.5-2 keV fluxes. They concluded that undetected absorption was responsible for the observed effect in unabsorbed sources. The magnitude of undetected absorption cannot be very significant in our *Lockman Hole* sources as we do not see a clear hardening of  $\langle \Gamma \rangle$  for unabsorbed sources. Using  $\Gamma$  and  $S$  from the APL model for unabsorbed sources we obtain the same result. Hence, if we still have sources with undetected absorption, their absorbing column densities cannot be very high. Moreover, we do not find evidence for the existence of a population of faint sources with intrinsically harder spectral slopes.

The results for the hard fluxes do not vary significantly from what we obtained with the SPL fits. This is exactly what we would expect if absorption produces the hardening of  $\Gamma$ , because the 2-10 keV fluxes are less affected by absorption.

In Fig. 6 we plot the values of absorption (observer's frame) that we obtained with the APL model, as a function of the 0.5-2 and 2-10 keV fluxes. There is an obvious correlation between the absorption and the observed soft flux. We see that the distribution of absorbing column densities does not seem to vary with the hard band fluxes. We have studied the dependence of  $N_{\text{H}}^{\text{obs}}$  with the 0.5-2 keV flux using de-absorbed fluxes, i.e. the 0.5-2 keV fluxes corrected for the effect of absorption. We found that when de-absorbed fluxes are used,  $N_{\text{H}}^{\text{obs}}$  does not

vary with X-ray flux, i.e., fainter and/or more distant objects do not appear to be more absorbed.

We have studied whether the fraction of X-ray absorbed objects depends on the flux after correcting for the effect of absorption (the  $N_{\text{H}}$  columns measured in our sample of sources are not high enough as to affect significantly the measured 2-10 keV fluxes and hence the correction of 2-10 keV fluxes for the effect of absorption is not significant). The results are plotted in Fig. 7. For comparison we have plotted the results that we obtain when absorbed fluxes are used (circles). We do not see significant differences using absorbed or de-absorbed 2-10 keV fluxes, because as explained before, these are not significantly affected by the absorption measured in our sources. However important differences are seen when 0.5-2 keV fluxes are used. If we do not correct for the effect of absorption in the 0.5-2 keV flux, we see an increase in the fraction of absorbed objects at fainter fluxes. However, if de-absorbed fluxes are used instead, the fraction of absorbed objects does not vary with the X-ray flux and we obtain the same result as in the 2-10 keV band.

Note that the fraction of absorbed sources at the faintest de-absorbed 0.5-2 keV fluxes ( $\sim 20\%$ ) is significantly lower than the values found at brighter fluxes. The absorbed sources that should contribute to the bin at the faintest fluxes have an observed flux below the threshold applied to our objects and therefore are not included in our sample (remember that to select our sources we used 0.2-12 keV counts, i.e.  $\sim$ fluxes without correction for absorption). Another effect that could also contribute to this result is that at the faintest fluxes we may have some sources with undetected absorption. We do not expect this effect to be important, because as we see in Fig. 5  $\langle \Gamma \rangle$  for unabsorbed sources does not seem to become significantly harder at the faintest 0.5-2 keV fluxes.

## 9. Best fit model

Up to now we have shown the results from spectral fits where only the X-ray continuum and the intrinsic absorption were modelled. However, there are other spectral components that



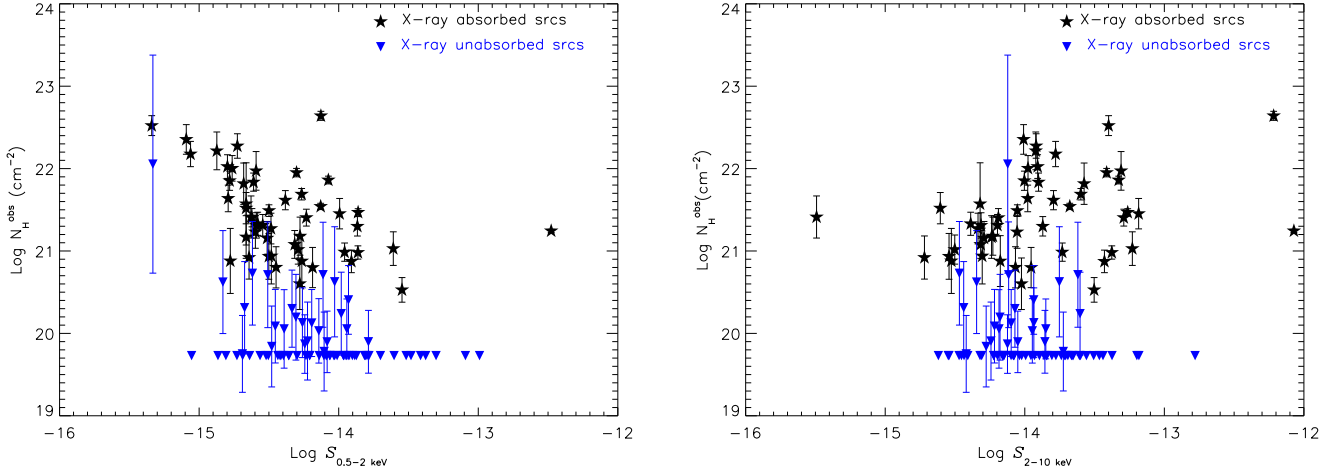


**Fig. 6.** Distribution of  $N_{\text{H}}^{\text{obs}}$  for absorbed (F-test  $\geq 95\%$ ; squares) and unabsorbed (F-test  $< 95\%$ ; triangles) objects. Error bars correspond to 90% confidence.

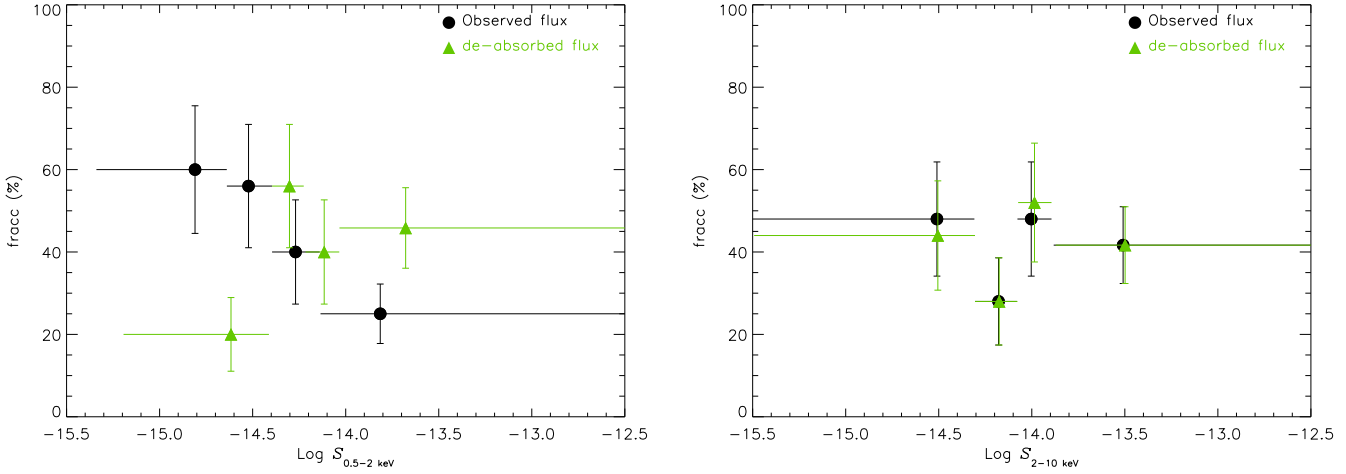


**Fig. 7.** Fraction of absorbed (F-test  $\geq 95\%$ ) objects vs 0.5-2 (left) and 2-10 (right) keV flux. For each source we used the fluxes from its best fit model (single power law or absorbed power law). Circles show the results that we obtained using observed fluxes, while the triangles show the results using fluxes corrected for the effect of absorption. See Sec. 8 for details.

**Table 2.** Results from the X-ray spectral analysis.

Model <sup>a</sup>	Total	type-1 AGN	type-2 AGN	Not id. <sup>b</sup>
SPL	65	35	5	25
SPL + SE	4	4	0	0
APL	39	6	16	17
APL + SE	5	0	4	1
CAPL	9	1	3	5
2SPL	1	0	0	1
Total	123	46	28	49

<sup>a</sup> Best fit model: SPL: single power law; APL: Absorbed power law; SE: Soft excess; CAPL: partial covering; 2SPL: two power laws (see Sec. 9 for details).

<sup>b</sup> Objects without optical identifications.

can also contribute significantly to the emission in the 0.2-12 keV energy band. There is evidence for them in the results that

we have shown previously. For example we see in Fig. 5 that  $\langle \Gamma \rangle$  seems not to vary with the X-ray flux when absorption is included in the fitting model. However we still have a clear scatter in the points which cannot be explained if  $\Gamma$  does not vary significantly with flux for the objects in our sample as our results appear to show. However, we would expect this scatter of  $\langle \Gamma \rangle$  if other spectral components are present in the data (e.g. soft excess emission) and they are not properly modelled. Besides the soft excess, other spectral components that can contribute to the 0.2-12 keV emission are ionised absorption, the Fe  $K\alpha$  emission complex and the Compton reflection hump that should appear at high X-ray energies.

We have studied in detail the MOS and pn time averaged spectra of each individual object. To model the soft excess emission we have used a black-body model. This component adds two free parameters to the fit, the temperature (in keV) and normalisation of the black-body. For some objects we could not

get a good fit of the detected soft excess with a black-body. In all these cases we obtained a good fit using a partial covering model (i.e., only part of the X-ray emission from the inner most region of the AGN is absorbed) to fit the signatures of absorption and soft excess emission. This model introduces one new parameter to the fit with respect to the APL model, the covering fraction of the absorber (between 0 and 1). The only emission line that we expect to detect with the quality of our spectra is the Fe  $K\alpha$  complex at 6.4 keV (rest frame energy for neutral iron). To search for this component we have used a Gaussian line profile, that allows us to calculate the centroid (in most cases we fixed the centroid to 6.4 keV), width and normalisation of the line. Absorption signatures found in some spectra were modelled with an absorption edge (zedge in xspec). This model introduced two free spectral parameters, the threshold energy and the absorption depth at the threshold energy. The most prominent signature from reflection in AGN is a change in the slope of the X-ray continuum at energies above 10 keV (rest frame). This component is known as the Compton reflection hump. We do not expect our objects to be bright enough as to detect with high significance reflection signatures given the limited bandpass of *XMM-Newton*. However, we have searched for this component in all the spectra adding a second power law to the fits at high energies.

The best fit model for each source is the one that gave a significant improvement in fit over the previous one in the sequence SPL-APL (with z in the case of identified sources)-APL+soft excess. The improvement in the fit was measured by the usual F-test, taking into account the improvement in the  $\chi^2$  value and the number of new parameters introduced. For some objects with soft excess emission, the detection of absorption was only significant after modelling of this spectral component. In particular, when the classification (type-1/type-2 AGN) of the identified sources is used, the parameters from the APL model with intrinsic absorption are always used.

Our results are listed in Table 2. The best fit spectral parameters obtained for each object are shown in Table 8. In the present paper we identify our objects with the numbers that will be used in a forthcoming catalogue paper of the *Lockman Hole* (H. Brunner et al. 2005, in preparation). The results were obtained fitting MOS and pn spectra simultaneously. If it was not required by the data we used the same MOS and pn model normalisations. For the sources for which we used different MOS and pn normalisations we show fluxes and luminosities obtained with the spectrum with best quality.

For 65 objects ( $\sim 53\%$ ) the best fit model was a single power law. Among these objects there were 35 type-1 AGN and 5 type-2 AGN. We detected absorption in 53 objects out of 123 (43%), including 7 type-1 AGN and 23 type-2 AGN. In Table 3 we list the fraction of absorbed objects in our sample and in the samples of type-1 and type-2 AGN. The values were corrected for spurious detections <sup>7</sup> following the method described in Mateos et al. (2005). We used the method described in Stevens et al. (2005) and Mateos et al. (2005) to compare the fraction of

<sup>7</sup> We accepted the spectral signatures as being real if the significance of detection from the F-test was  $\geq 95\%$ . Hence 5% of detections are expected to be spurious.

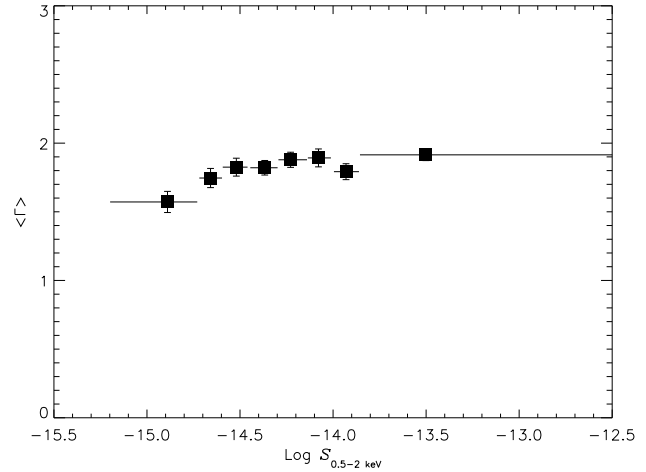


**Fig. 8.** Dependence  $\langle \Gamma \rangle$  with 0.5-2 keV flux. For each source we used the spectral parameters obtained from its best fit model (see Sec. 9 for details).

absorbed objects in type-1 and type-2 AGN. We find that these fractions are different (the number of absorbed objects in type-2 AGN being larger than in type-1 AGN) with a significance of more than 99.99%.

**Table 3.** Results of detection of X-ray absorption.

	$N_{\text{tot}}$	$N_{\text{abs}}$	$f^{\text{a}}$	$f_{\text{lim}}^{\text{b}}$
All sources	123	53	0.38	$\geq 0.27$
type-1 AGN	46	7	0.10	$\leq 0.29$
type-2 AGN	28	23	0.77	$\geq 0.51$

<sup>a</sup> Fraction of absorbed objects taking into account the expected fraction of spurious detections (see Sec.9)

<sup>b</sup>  $3\sigma$  limits in the fraction of absorbed objects

### 9.1. Broad band continuum

Using the best fit spectral slopes we obtained a weighted  $\langle \Gamma \rangle$  for the objects in our sample of  $1.87 \pm 0.02$  ( $1.86 \pm 0.02$  if the arithmetic mean is used). In Fig. 8 we show the dependence of  $\langle \Gamma \rangle$  with the 0.5-2 keV flux using the best fit parameters ( $\Gamma$  and  $S$ ) for each object (the same result is obtained using 2-10 keV fluxes). We see that when we take into account during fitting all the spectral components, the scatter in  $\langle \Gamma \rangle$  (see Fig. 5) is reduced significantly, and most of the points are consistent with the obtained average value of  $\Gamma$ .

The mean spectral slope was found to be  $1.89 \pm 0.03$  ( $1.88 \pm 0.03$  with the arithmetic mean) for type-1 AGN and  $1.71 \pm 0.03$  ( $1.82 \pm 0.06$  with the arithmetic mean) for type-2 AGN. In Fig. 9 we compare  $\langle \Gamma \rangle$  for type-1 and type-2 AGN as a function of the X-ray fluxes. For type-1 AGN, where only 7 out of 46 are X-ray absorbed, we obtain the same results using 0.5-2 and 2-10 keV fluxes, i.e., no dependence of  $\langle \Gamma \rangle$  with the X-ray flux. However, X-ray absorption is important in type-2 AGN ( $\geq 50\%$  of type-2

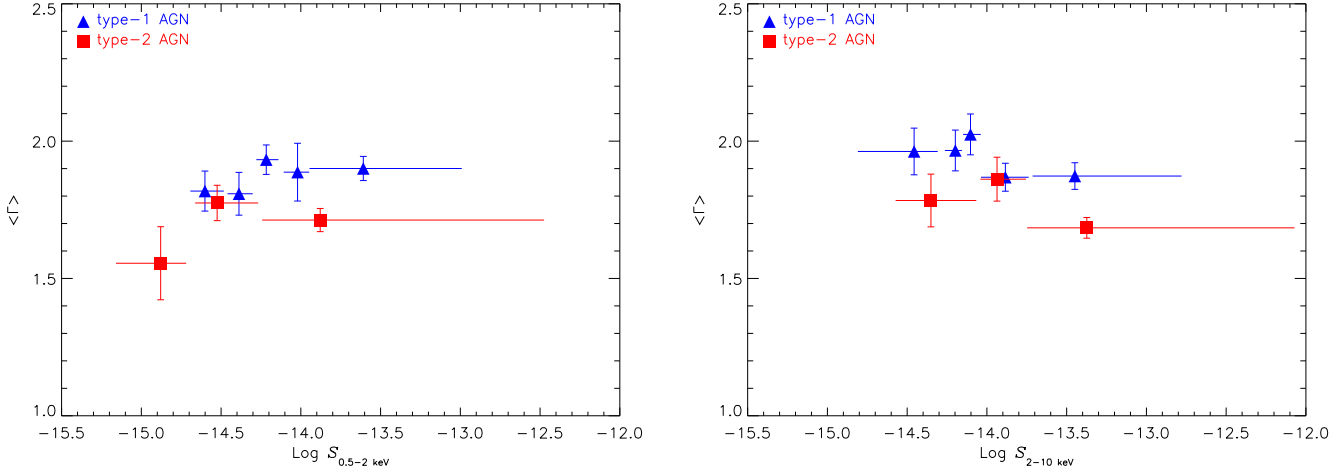


**Fig. 9.** Dependence of  $\langle \Gamma \rangle$  with 0.5-2 and 2-10 keV flux for type-1 and type-2 AGN. For each source we used  $\Gamma$  and  $S$  from its best fit model (single power law or absorbed power law). See Sec. 9.1 for details.

AGN being X-ray absorbed). The ratio of type-2 AGN/type-1 AGN increases as we go to fainter 0.5-2 keV absorbed (i.e. not absorption corrected) fluxes, while it remains constant with 2-10 keV flux. We explained in detail in Sec. 6 that this is due to the existing correlation between  $N_{\text{H}}$  and the soft absorbed flux, i.e. most absorbed objects have the faintest fluxes in the 0.5-2 keV band. We see in Fig. 9 that there is a clear dispersion in  $\langle \Gamma \rangle$  for type-1 and type-2 AGN, however it seems that type-2 AGN tend to have lower  $\langle \Gamma \rangle$  than type-1 AGN at the fluxes covered by our sample. Excluding from the sample of type-2 AGN the three sources that we found with no detected X-ray absorption and spectral slope significantly lower than the average value for type-1 AGN (see Sec. 11 and Table 7), we still see the same dependence of  $\langle \Gamma \rangle$  with X-ray flux for type-2 AGN.

We have followed the procedure described in Nandra & Pounds (1994) and Maccararo et al. (1988) to estimate the intrinsic dispersion of the photon index in type-1 and type-2 AGN, and to investigate whether after allowing for intrinsic dispersion in  $\Gamma$ , we still find type-2 AGN to be on average flatter than type-1 AGN. In this method it is assumed that the dispersion in  $\Gamma$  values can be described well with a Gaussian function of mean  $\langle \Gamma \rangle$  and dispersion  $\sigma_{\langle \Gamma \rangle}$ . The results of this analysis are listed in Table 4, where we have the values obtained using the weighted mean for comparison. We have found that there is an intrinsic dispersion in  $\Gamma$  of  $\sim 0.2$  in type-1 AGN and type-2 AGN, and that the value of the dispersion is similar in both samples of objects. It is interesting to note that the results obtained with the weighted mean and the Maximum Likelihood method are consistent within each other.

In Fig. 10 we show the contours in  $\langle \Gamma \rangle$ - $\sigma_{\langle \Gamma \rangle}$  space for a  $\Delta\chi^2$  of 2.3, 6.17 and 11.8 that correspond to 1, 2 and  $3\sigma$  for two parameters. The significance of type-2 AGN being on average flatter than type-1 AGN is only at  $1.62\sigma$  (using the values of  $\Gamma$  obtained with the ML method<sup>8</sup>).

<sup>8</sup> Note that the significance of  $\Gamma$  being different for type-1 AGN and type-2 AGN is  $\sim 4\sigma$  if the values obtained with the weighted mean are used and no intrinsic dispersion in  $\Gamma$  is considered

However, it is important to note that if the signatures of absorption in the X-ray spectra are not very significant, the detected values of  $N_{\text{H}}$  will tend to be lower than the real ones (see Mateos et al. 2005) and then, the fitted  $\Gamma$  will be flatter. We expect this effect to be more important for type-2 AGN where we have more sources with absorption. The small difference in  $\langle \Gamma \rangle$  for type-1 and type-2 AGN might be due to this effect. Therefore with the current data we cannot reach any strong conclusion.

## 9.2. X-ray absorption

We have detected X-ray absorption in  $\sim 37\%$  of the sources in our sample. Absorption was found in  $\sim 10\%$  of type-1 AGN and  $\sim 77\%$  of type-2 AGN. We first checked that the measured  $\Gamma$  and  $N_{\text{H}}$  were not correlated, and therefore that we have obtained reliable parameters, especially the column density for each individual object. The results are plotted in Fig. 11 for sources with known redshifts, where we do not see any evident correlation between the two spectral parameters. In the objects with large  $\Gamma$ , the values including the error bars are in all cases consistent with a value of  $\Gamma \sim 2$ .

**Table 4.** Mean spectral photon index of type-1 and type-2 AGN obtained with the weighted and arithmetic means and with the Maximum Likelihood analysis. The spectral slopes from the sources' best fit model were used.

Sample	Maximum Likelihood $\langle \Gamma \rangle$	Maximum Likelihood $\sigma$	Weighted Mean	Arithmetic Mean
Whole sample	$1.92^{0.03}_{0.18}$	$0.28^{0.04}_{0.13}$	$1.87 \pm 0.02$	$1.86 \pm 0.02$
type - 1 AGN	$1.89^{0.06}_{0.05}$	$0.20^{0.04}_{0.04}$	$1.89 \pm 0.03$	$1.88 \pm 0.03$
type - 2 AGN	$1.72^{0.10}_{0.08}$	$0.20^{0.10}_{0.07}$	$1.71 \pm 0.03$	$1.82 \pm 0.06$

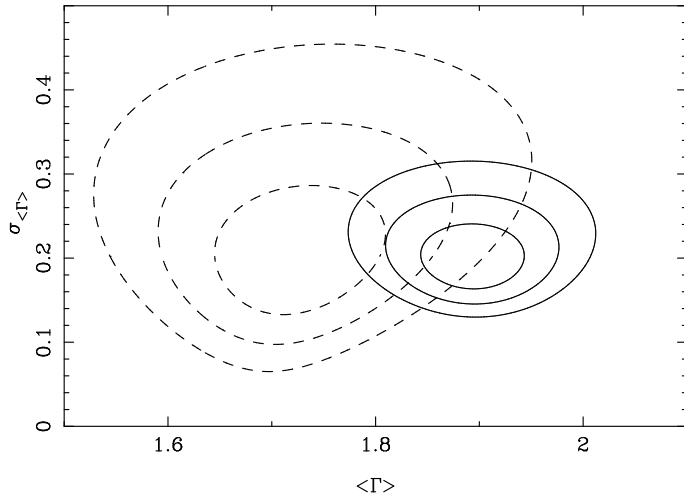


**Fig. 10.** Contour diagrams for the value of the average spectral slope and intrinsic dispersion of our samples of type-1 AGN (solid lines) and type-2 AGN (dashed lines) obtained from the Maximum Likelihood analysis (see Sec. 9). The contours are defined as  $\Delta\chi^2=2.3, 6.17$  and  $11.8$  corresponding to standard 1, 2 and  $3\sigma$  confidence regions for two parameters.

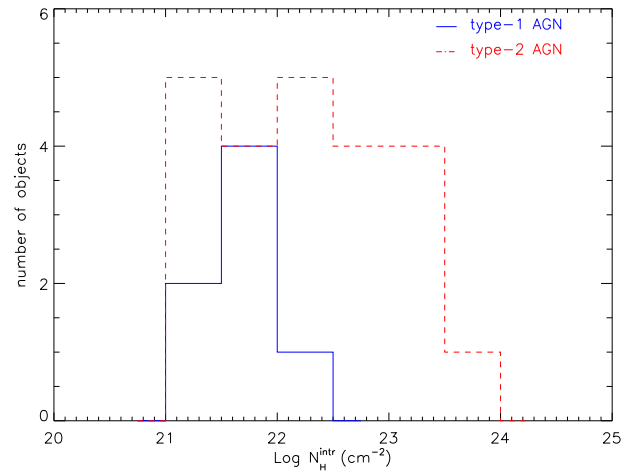


**Fig. 12.** Distributions of intrinsic (rest frame) absorption in type-1 and type-2 AGN obtained from the best fit model for sources.

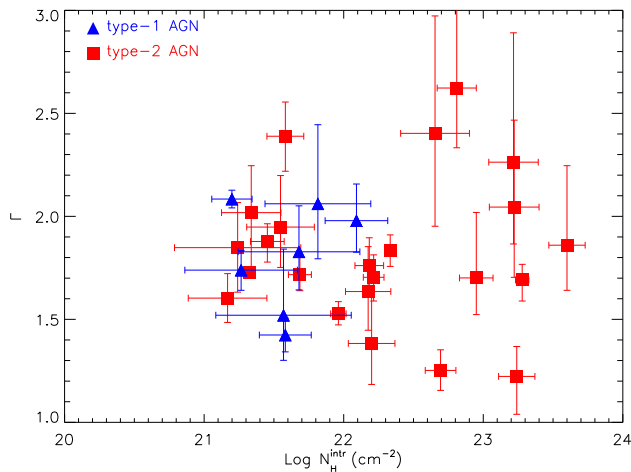


**Fig. 11.**  $\Gamma$  vs.  $N_{\text{H}}^{\text{intr}}$  (rest-frame) for the type-1 and type-2 AGN with detected absorption. Note that all type-1 AGN have column densities between  $10^{21} - 10^{22} \text{ cm}^{-2}$  while type-2 AGN have a much wider distribution of  $N_{\text{H}}^{\text{intr}}$ .

Note in Fig. 11, that the  $N_{\text{H}}^{\text{intr}}$  distributions in type-1 and type-2 AGN seem to be different. The measured column densities in absorbed type-1 AGN are between  $10^{21} - 10^{22} \text{ cm}^{-2}$ , while type-2 AGN have a much wider distribution of values, many objects having  $N_{\text{H}}^{\text{intr}} \geq 10^{23} \text{ cm}^{-2}$ . We show the distributions of  $N_{\text{H}}^{\text{intr}}$  in type-1 and type-2 AGN in Fig. 12. The distributions appear to be different, with type-2 AGN being in general more absorbed than type-1 AGN. Using the KS test to compare the two distributions we obtained a probability of them being different of  $> 92\%$ . We will have to wait for the analysis of the faint sample of objects before reaching a stronger conclusion.

In terms of the unified model of AGN, X-ray absorption and optical obscuration should be correlated. There is observational

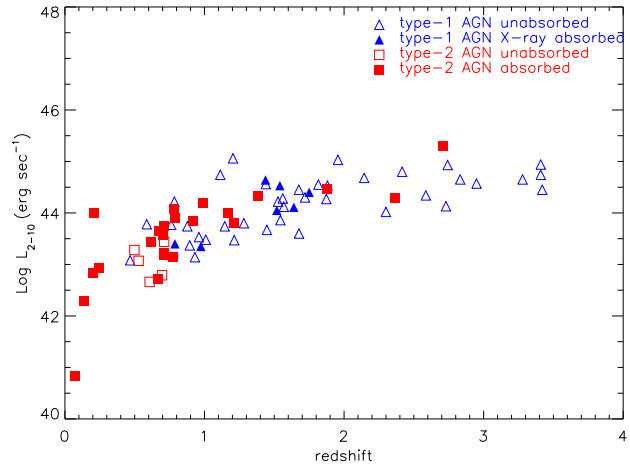


**Fig. 13.** 2-10 keV luminosity (corrected for absorption) vs. redshift for type-1 and type-2 AGN. Absorbed sources are the objects where we found an F-test significance of improvement of the fits  $\geq 95\%$ .

evidence that this does not hold for all AGN, although only a few cases are based on a proper spectral analysis. We can confirm that these discrepancies exist in a significant fraction of our objects. Mateos et al. (2005) found some indications that the AGN/host galaxy contrast effect<sup>9</sup> might explain why broad optical lines are not observed in unabsorbed type-2 AGN. In Fig. 13 we show the redshift distribution of the AGN in our sample. Because our sample of AGN is much smaller we can not perform a similar test.

<sup>9</sup> In the redshift interval where the distributions of type-1 and type-2 AGN overlapped, they found that unabsorbed type-2 AGN were less luminous than type-1 AGN

**Table 5.** Properties of the soft excess emission in type-1 and type-2 AGN that was modelled with a black body.

ID	Class	redshift	( $L_{\text{BB}}/L_{\text{PO}}$ ) (0.5 – 2 keV)	kT (eV)	$L_{\text{BB}}$ (0.5 – 2 keV)	L (2 – 10 keV)
(1)	(2)	(3)	(4)	(5)	(6)	(7)
90	type – 1 AGN	0.467	0.363	$105^{+17}_{-20}$	42.64	43.08
148	type – 1 AGN	1.113	0.479	$78^{+6}_{-8}$	44.44	44.74
270	type – 1 AGN	1.568	0.426	$109^{+10}_{-15}$	43.80	44.12
342	type – 1 AGN	0.586	0.081	$67^{+3}_{-7}$	42.79	43.78
259	type – 2 AGN	0.792	0.063	$291^{+149}_{-90}$	42.11	43.90
290	type – 2 AGN	0.204	0.035	$188^{+17}_{-15}$	41.32	42.83
424	type – 2 AGN	0.707	0.060	$474^{+26}_{-153}$	42.25	43.74
511	type – 2 AGN	0.704	0.014	$83^{+87}_{-38}$	42.12	43.58

Columns are as follows: (1) Source X-ray identification number; (2) object class based on optical spectroscopy; (3) redshift; (4) ratio of soft excess to power law 0.5-2 keV luminosities (this ratio is frequently used to measure the strength of the soft excess emission); (5) temperature of the soft excess (using a black-body model); (6) logarithm of the 0.5-2 keV luminosity of the soft excess component; (7) logarithm of the 2-10 keV luminosity of the power law component (for absorbed sources the luminosity was absorption corrected).

### 9.3. Soft excess

We detected soft excess emission ( $\geq 95\%$  confidence limit from an F-test) in 18 (15%) objects. The number of MOS+pn counts in the soft excess component vary from 100 to 1000 except for one source where the soft excess component has  $\sim 3000$  counts. Within the sources classified as AGN we found soft excess in 5 (11%) type-1 AGN and 7 (25%) type-2 AGN. The significance of the fractions of type-1 and type-2 AGN with detected soft excess emission being different is 97%.

Although our results suggest that soft excess emission might be more common in type-2 AGN, it is important to note that our samples of type-1 and type-2 AGN have different redshift distributions, and for the highest redshift sources (all type-1 AGN) we expect most of the signatures of soft excess emission to be redshifted outside the observed energy interval, making the detection of soft excess more difficult. Therefore, we have repeated the comparison using only sources in the redshift interval where we detected soft excess ( $z < 1.568$ ). In this case, the significance of the fractions of type-1 and type-2 AGN with detected soft excess emission being different is reduced to 87%. Hence, with our data we cannot confirm that soft excess emission is more common in type-2 AGN than in type-1 AGN.

In 9 sources (4 type-1 AGN, 4 type-2 AGN and 1 unidentified object) we fitted the soft excess emission with a black body model (a Raymond Smith model gave an equally good fit). The properties of the soft excess, i.e. temperature, 0.5-2 keV luminosity and strength, for the identified sources are listed in Table 5. We see that the measured black-body properties do not depend on the 2-10 keV X-ray luminosity of the objects. For the unidentified object with detected soft excess fitted with a black body we found an observed black body temperature of  $0.164^{+0.046}_{-0.033}$  eV.

The average temperature of the black body was found to be  $0.09 \pm 0.01$  keV for type-1 AGN and  $0.26 \pm 0.08$  keV for type-2 AGN. The average 0.5-2 keV luminosities of the black body (in log units) were  $43.42 \pm 0.43$  erg  $s^{-1}$  for type-1 AGN and  $44.11 \pm 0.44$  erg  $s^{-1}$  for type-2 AGN. The 0.5-2 keV luminosities of the soft excess component in type-1 and type-2 AGN

were not found to be significantly different (a KS test of the luminosity distributions gave a significance of them being different of only 90%). However the measured temperatures of the soft excess were found to be higher in type-2 AGN than in type-1 AGN. This could be because the soft excess in type-2 AGN might contain a fraction of scattered radiation. We also see that in most sources the temperatures of the black body are well above 60 eV<sup>10</sup>, and hence it is difficult to explain the origin of the soft excess emission in these sources as thermal emission from the accretion disc. Comptonization of cool photons in a cloud of hot electrons surrounding the accretion disc might be an alternative explanation.

In 9 other objects (1 type-1 AGN, 3 type-2 AGN and 5 unidentified objects) the black body could not fit the signatures of the soft excess. An alternative method for modelling the curvature at soft energies is a scattering or partial covering model (pcfabs in xspec). The model consists of the sum of two power law components having the same spectral index, but affected by different absorption (quantified with the covering fraction parameter). This model improved significantly the quality of the fits, and provided a good fit of the soft excess emission in all sources. The average covering fraction that we obtained was  $0.82 \pm 0.06$  (the maximum and minimum values being 0.98 and 0.50). This value implies that the scattering fraction in these sources is rather large ( $18 \pm 6\%$ ).

### 9.4. Reprocessed components

We have searched for a flattening of the continuum at high energies (i.e. Compton reflection) adding a second power law to the model. We have found signatures of spectral hardening at high energies in only one object, source 108, which is still unidentified. The unfolded MOS and pn spectra of this source are shown in Fig. 14. We first fitted the X-ray spectrum of this object with a single power law giving  $\Gamma \sim 1.5$  but the fit was poor, with a  $\chi^2$  of 127 for 67 degrees of freedom. We found that

<sup>10</sup> The hottest thermal emission expected from an accretion disc surrounding a  $10^6 M_{\odot}$  black hole.

**Table 6.** Parameters of the Gaussian line in the six identified sources where signatures of line emission were detected with an F-test significance  $\geq 95\%$ .

ID	Class	redshift	$L_{2-10}$	Line	$\sigma$	Equivalent	F – test
(1)	(2)	(3)	erg s <sup>-1</sup>	energy (keV)	(keV)	width (eV)	prob. (%)
(1)	(2)	(3)	(4)	(5)	(6)	(7)	(8)
270	type – 1 AGN	1.568	44.12	6.24 <sup>+0.48</sup> <sub>-0.08</sub>	0.00 <sup>+0.82</sup> <sub>-0.00</sub>	452	99
21	type – 2 AGN	0.498	43.28	5.90 <sup>+0.92</sup> <sub>-1.64</sub>	0.56 <sup>+2.19</sup> <sub>-0.45</sub>	1462	95
172	type – 2 AGN	1.170	44.00	6.40 <sup>+1.87</sup> <sub>-0.41</sub>	0.09 <sup>+2.93</sup> <sub>-0.00</sub>	360	99
290	type – 2 AGN	0.204	42.83	6.32 <sup>+0.07</sup> <sub>-0.61</sub>	0.00 <sup>+0.14</sup> <sub>-0.00</sub>	283	96
326	type – 2 AGN	0.780	44.08	6.59 <sup>+0.06</sup> <sub>-0.09</sub>	0.02 <sup>+2.12</sup> <sub>-0.00</sub>	224	99
407	type – 2 AGN	0.990	44.20	6.40 <sup>+0.10</sup> <sub>-0.43</sub>	0.40 <sup>+0.10</sup> <sub>-0.18</sub>	653	> 99.99

Columns are as follows: (1) Source X-ray identification number; (2) optical class based on optical spectroscopy; (3) redshift; (4) 2-10 keV luminosity; (5) and (6) rest-frame centroid energy and width of the emission line; (7) rest-frame equivalent width of the line; (8) F-test significance for the detection of the line.

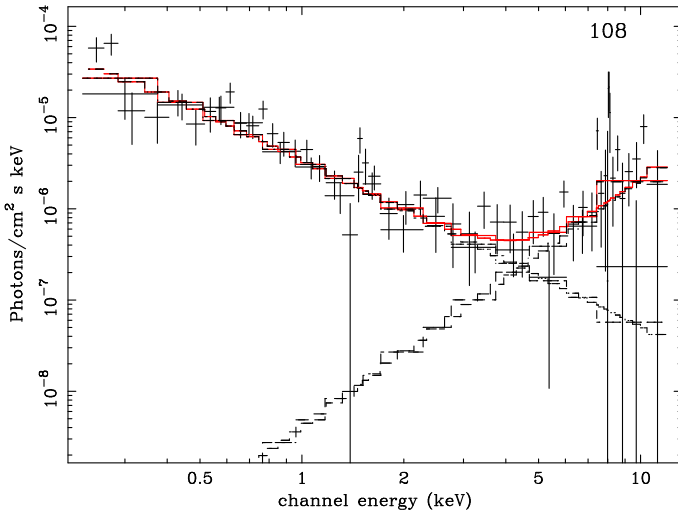


**Fig. 14.** Unfolded MOS and pn spectrum of the only source in the sample where we detected a hardening in the X-ray continuum emission at high energies (Compton reflection hump). Because this object is still unidentified we fitted the hard spectral component with a second power law. The F-test significance of this component was found to be 99.98%.

there was a clear excess emission at high energies. We then fitted the spectrum with two power laws, and the  $\chi^2$  significantly decreased to 98 for 65 degrees of freedom. The F-test significance of improvement of the fit with the new component was 99.98%. In this case we obtained a value of  $\Gamma$  of  $1.83 \pm 0.17$  for the continuum emission flattening out to  $\Gamma = -2.56^{+0.61}_{-0.19}$  at high energies. We did not find evidence for X-ray absorption or emission lines in the spectrum of this source. We will have to wait until we have the optical identification of this source before saying more about the X-ray emission of this object.

Another signature of reprocessing that has been found in many spectra of AGN is an emission line around 6.4 keV. This is interpreted as Fe K $\alpha$  fluorescence from cold matter (Pounds et al., 1989,1990; Nandra et al., 1991; Nandra & Pounds 1994) and might originate from the reprocessing of hard X-ray photons in the accretion disc (Pounds et al. 1990).

We have searched for this component in our sources using a Gaussian model. Most time averaged spectra of our sources do not have enough signal to noise as to detect Fe K $\alpha$  line emission. However, we have been able to detect signatures of line emission with an F-test significance  $\geq 95\%$  in the MOS and pn spectra of 8 objects (1 type-1 AGN, 5 type-2 AGN and 2 unidentified sources). In Fig 15 we show the MOS+pn unfolded time averaged spectra of these sources. The parameters of the Gaussian line for each identified source are listed in Table 6.

**Sources 21 and 407:** In these sources we found a significant width in the line profile, which might be indicating that the line was formed in the inner parts of the accretion disc, and hence it should have a relativistic profile (with a red wing component due to gravitational redshift). When fitted with a Gaussian model, we would expect the line centroid to be found at an energy slightly below 6.4 keV. While in source 407 the line centroid is consistent with being neutral iron, in source 21 it was  $\sim 5.9$  keV (although consistent with being neutral iron within the error bars).

**Sources 270 and 290:** In these sources we detected a narrow Gaussian line and line centroids lower (but consistent within the error bars) than the value for neutral iron.

**Sources 172 and 326:** In these sources we also found a significant line width, although in both cases it was consistent with zero at 90% confidence. In source 172 the line centroid was consistent with being neutral iron, but in source 326 it was significantly higher (even within the error bars). In this source the line might be originating in an ionised accretion disc.

In all the spectra where we detected the line we did not have enough signal to noise in the data in order to use a more physical model to fit the profile of the line (*xspec* models *laor* for a Kerr black hole or *diskline* for a Schwarzschild black hole). The rest frame equivalent width (EW) of the line in the type-1 AGN where we detected this component was found to be  $\sim 452$  eV. In most type-2 AGN the measured values were between 200 and 600 eV. However there is one source, 21 for which we found a rest frame EW of  $\sim 1400$ , substantially higher than in the other type-2 AGN. It is important to note that in this source the F-test significance of detection of line was the lowest

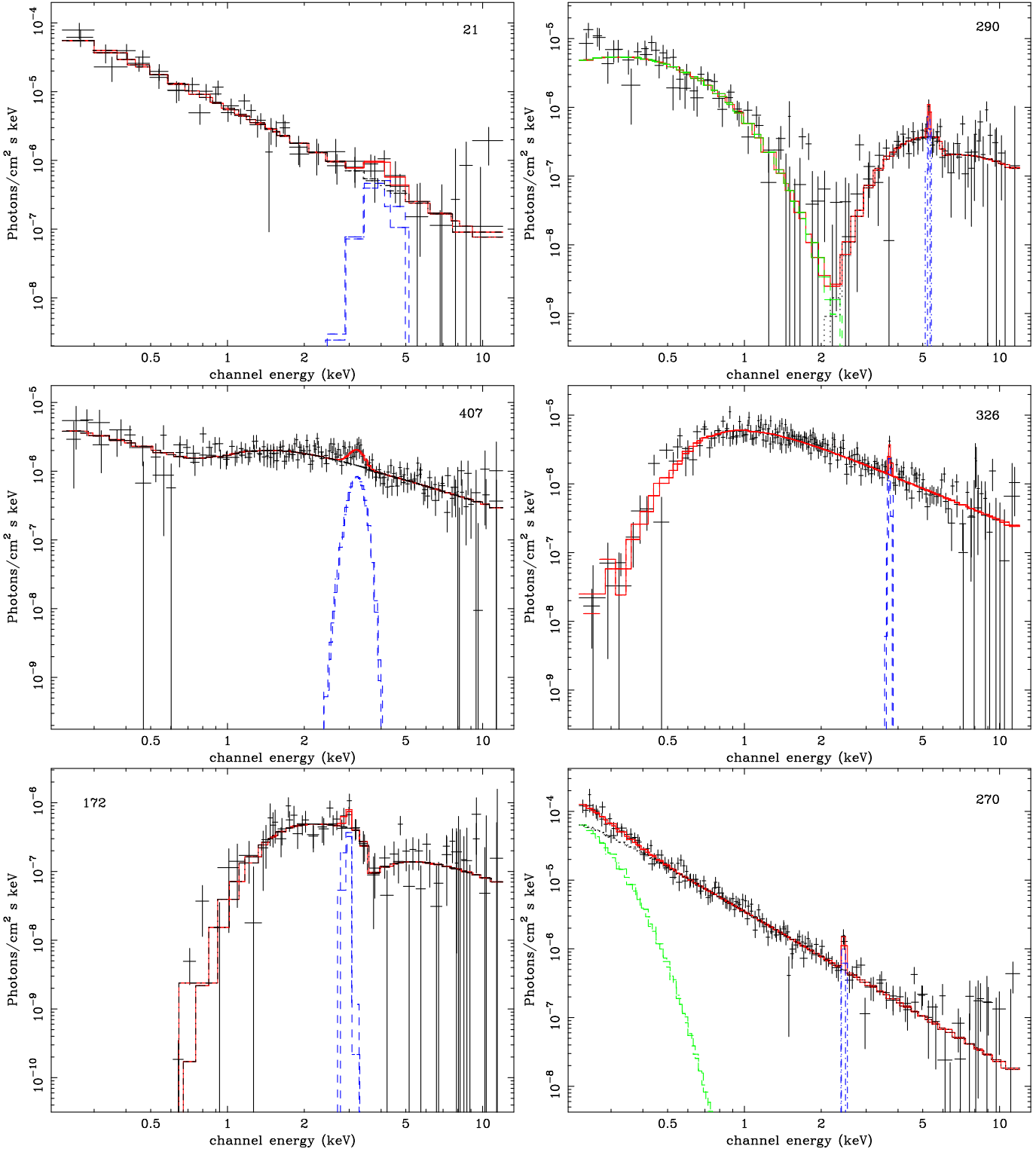


**Fig. 15.** Unfolded MOS and pn time averaged spectra of the 6 AGN where we detected signatures of emission line at high energies (F-test significance  $\geq 95\%$ ). In the X-ray spectrum of source 172 (type-2 AGN) we also found an absorption edge at an energy of  $\sim 7.56_{0.76}^{0.54}$  keV with absorption depth  $\tau = 1.4_{0.6}^{0.8}$  (F-test significance of detection was 99%).

among all sources (95%) and hence the measured value has the highest uncertainty.

Using the same sample of objects, Streblyanska et al. (2005) found a clear relativistic line profile in the average rest-frame spectrum of type-1 and type-2 AGN. In objects with

broad Fe lines, the contribution of the broad component is difficult to detect if there is not enough signal to noise since its contribution is less than 10% above the continuum over most of the spectrum.



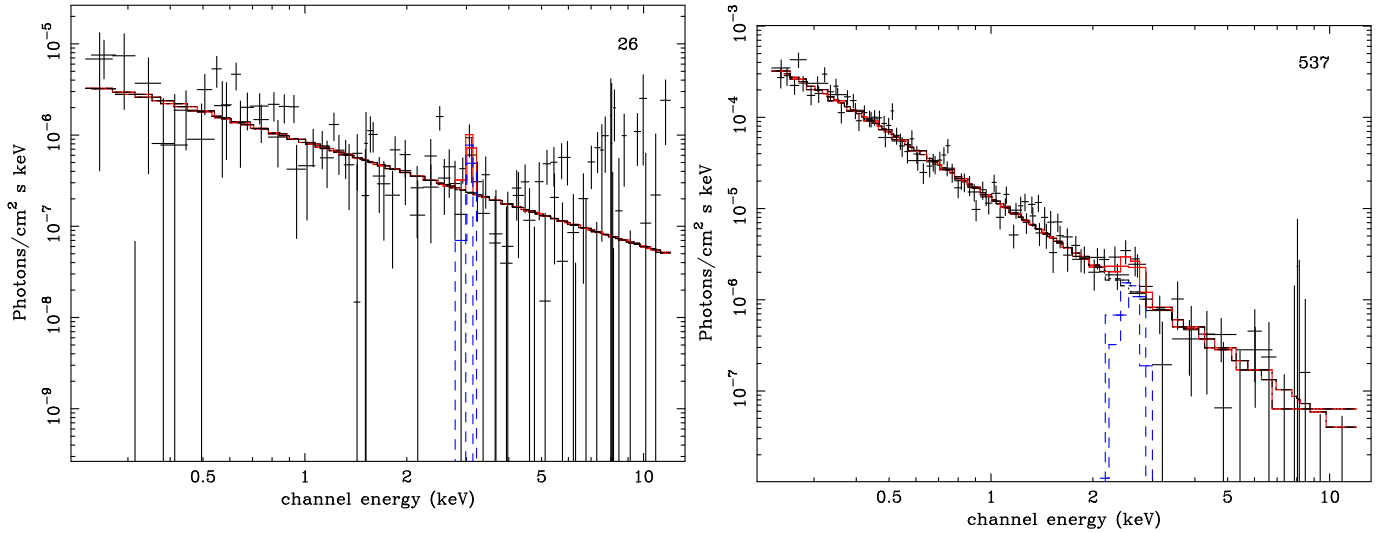


**Fig. 16.** Unfolded MOS and pn time averaged spectra of the two still unidentified sources (source numbers 26 and 537) where we detected signatures of emission line at high energies (F-test significance  $\geq 95\%$ ).

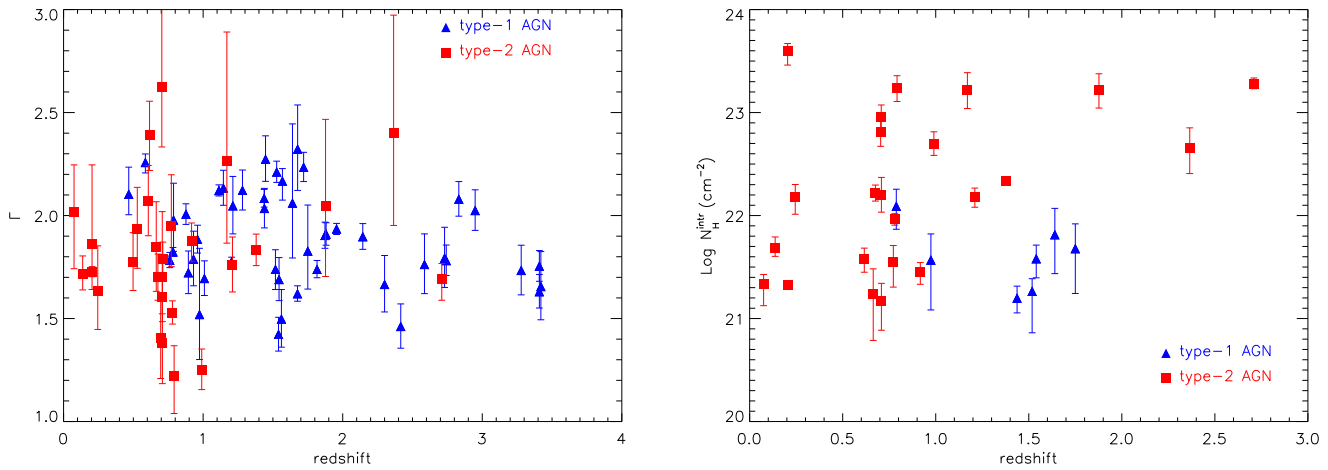


**Fig. 17.** Evolution with redshift of  $\Gamma$  and  $N_{\text{H}}^{\text{intr}}$  (rest-frame) for type-1 and type-2 AGN. Error bars correspond to 90% confidence

## 10. Dependence of sources spectra with luminosity and redshift

We show  $\Gamma$  and  $N_{\text{H}}^{\text{intr}}$  vs. redshift for type-1 AGN and type-2 AGN in Fig. 17. In these plots we can see the different redshift distributions between the type-1 and type-2 AGN in our sample. Most detected type-2 AGN have redshifts below 1, while we find type-1 AGN up to a redshift of  $\sim 3.5$ . We have applied a Spearman correlation test to search for evolution of  $\Gamma$  and  $N_{\text{H}}^{\text{intr}}$  with redshift. We found that the correlation between  $\Gamma$  and redshift is  $-0.22$  for type-1 AGN and  $-0.04$  for type-2 AGN. The significance of  $\Gamma$  being flatter at higher redshifts is 86% for type-1 AGN and 15% for type-2 AGN. The continuum shape of our sample of AGN does not seem to evolve with redshift, however the number of AGN at high redshift (specially the number of type-2 AGN) is too small to give a strong conclusion.

The same result is obtained when searching for correlation of  $N_{\text{H}}^{\text{intr}}$  with redshift, i.e. AGN at high redshift do not seem to be more absorbed than local ones. The apparent scarcity of

high redshift ( $z \geq 1$ ) low  $N_{\text{H}}$  sources is probably a selection effect, since it is easier to detect highly absorbed sources at high redshifts.

We have studied the dependence of  $\Gamma$  and  $N_{\text{H}}^{\text{intr}}$  with the 2-10 keV X-ray luminosity (we use the 2-10 keV luminosity because these values are less affected by X-ray absorption). The results are plotted in Fig 18. We do not see any correlation between the spectral slope and the column density of our AGN with 2-10 keV X-ray luminosity. Note in Fig. 18 that our sample contains 6 objects (all optically identified as type-2 AGN) that fall within the “standard” QSO2 region, i.e.,  $L_X \geq 10^{44}$  erg  $\text{s}^{-1}$  and  $N_{\text{H}}^{\text{intr}} \geq 10^{22}$   $\text{cm}^{-2}$ .

## 11. Unabsorbed type-2 AGN

We have found 5 objects identified as type-2 AGN but with no clear evidence of X-ray absorption in their X-ray spectrum ( $\sim 23\%$ , see Table. 3). In Fig. 19 we show the unfolded spectra of these sources obtained with their best fit model (in all the



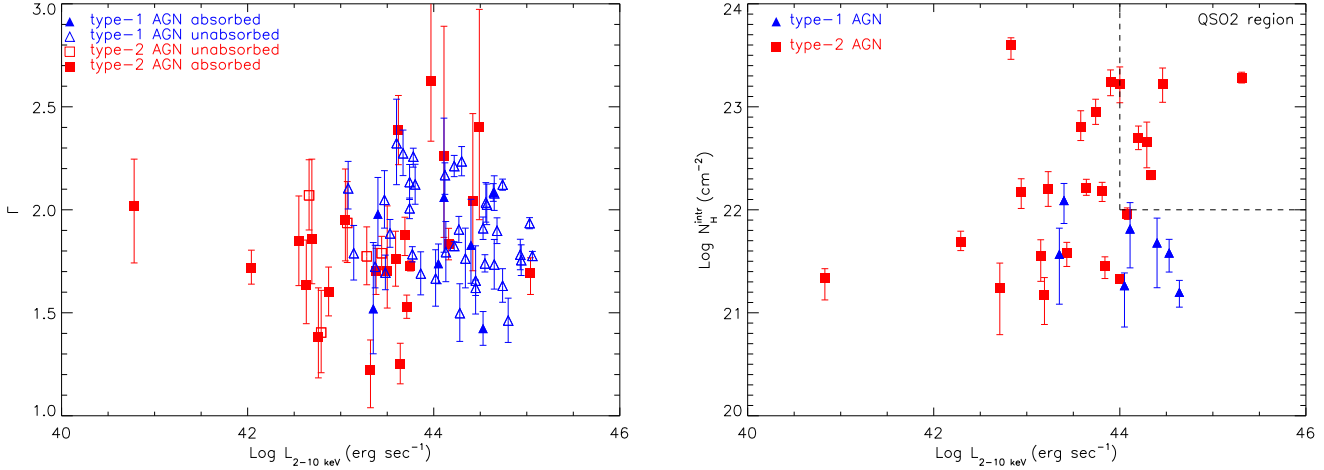


**Fig. 18.** Left:  $\Gamma$  vs. 2-10 keV luminosity. Right:  $N_{\text{H}}^{\text{intr}}$  vs. 2-10 keV luminosity for type-1 and type-2 AGN. In the  $N_{\text{H}}^{\text{intr}}$  vs. 2-10 keV plot we show the QSO2 region (defined as  $L_{2-10} \geq 10^{44} \text{ erg s}^{-1}$  and  $N_{\text{H}} \geq 10^{22} \text{ cm}^{-2}$ ) where we have 6 QSO2 candidates. Error bars correspond to 90% confidence

cases a single power law). Several authors have found AGN with weak or no broad emission lines in their optical spectrum and with unabsorbed X-ray spectra (see for example Pappa et al., 2001; Panessa et al., 2002; Barcons et al., 2003; Mateos et al., 2005; Carrera et al., 2004; Corral et al. 2005).

One possible explanation for these results is that the signal to noise of the spectra of these sources is not high enough to detect signatures of X-ray absorption (see e.g. Mateos et al., 2005). Our current data is however of sufficient quality to detect X-ray absorption or X-ray absorption+soft excess to weak levels. Moreover, as we see in Fig. 19 the time averaged spectra of these sources has enough signal to noise as to detect X-ray absorption with the column densities common in type-2 AGN. We have calculated the upper limits (at 90% confidence) to the X-ray absorption in these sources. They are listed in Table 7. The values that we obtain are lower than the typical column densities found in our absorbed type-2 AGN. If these sources are X-ray absorbed, the values for the column density that we have found are consistent with arising in absorption from their host galaxy.

Another possibility that might explain the lack of X-ray absorption in these sources is X-ray spectral variability. The optical and X-ray observations of these sources have not been obtained simultaneously, and the X-ray absorption in these sources might have changed with time. Corral et al. (2005) studied the hypothesis of spectral variability using simultaneous X-ray and optical observations of the Seyfert galaxy Mkn993. They found the source to be X-ray unabsorbed but in a type 1.9 optical. Results of a detailed study of X-ray flux and spectral variability on scales from months to years of the same sample of sources used for this work, will be presented in a forthcoming paper (Mateos et al. 2005b in preparation) where we show that X-ray variability cannot explain the lack of X-ray absorption in our unabsorbed type-2 AGN.

We have checked whether these sources can be Compton-thick type-2 AGN. If the torus is Compton-thick to optical scattering, even 2-10 keV photons will not be directly seen

and hence the direct radiation in these sources would be completely blocked. In some cases scattered radiation (with no apparent absorption) could be the only radiation seen below 10 keV. In Compton-thick sources, because the primary radiation is fainter, the equivalent width of the  $K\alpha$  line increases. Bassani et al. (1999) show a diagram of the EW versus the transmission parameter  $T$ , where  $T$  is  $S_{\text{X}}/S_{[\text{OIII}]}$ <sup>11</sup>. This diagram can be used to identify Compton-thick sources if the values of EW and  $T$  are known. We do not know the value of  $S_{[\text{OIII}]}$  for our sources, however we have measured the EW to check in which part of the diagram our sources fall. To measure the EW we added a Gaussian line representing the iron  $K\alpha$  emission to the spectrum of our sources. We fixed the centroid of the line to 6.4 and the width to 0 (the quality of the fits did not improve allowing the line parameters to vary). Only in source 21, there might be emission from iron  $K\alpha$  line (F-test significance  $\sim 95\%$ ). In the other sources there are no indications of iron  $K\alpha$  emission. The values of the EW that we have found are listed in column (6) of Table 7. In most of the cases we obtained a value of the EW below  $\sim 1500$ , and therefore these sources fall outside the region of Compton-thick sources in the Bassani et al. (1999) diagram. However, to confirm our results, specially for objects 21 and 476 with EW values above 1000 eV, we need a reliable measurement of the [OIII] flux.

## 12. Extragalactic X-ray background

The spectrum of the extragalactic X-ray background (XRB) was measured by the HEAO satellite (Marshall et al. 1980) from 1-50 keV. At these energies, the XRB spectrum can be reproduced well by an optically thin plasma of temperature  $\sim 40$  keV. At low energies,  $\leq 15$  keV, a good description of the data is obtained with a power law of  $\Gamma=1.4$ . The spectrum of the

<sup>11</sup>  $S_{\text{X}}$  is the X-ray flux and  $S_{[\text{OIII}]}$  is the optical flux of the [OIII]  $\lambda 5007$  emission line. [OIII]  $\lambda 5007$  has been frequently used as an isotropic indicator of the intrinsic brightness of the sources.

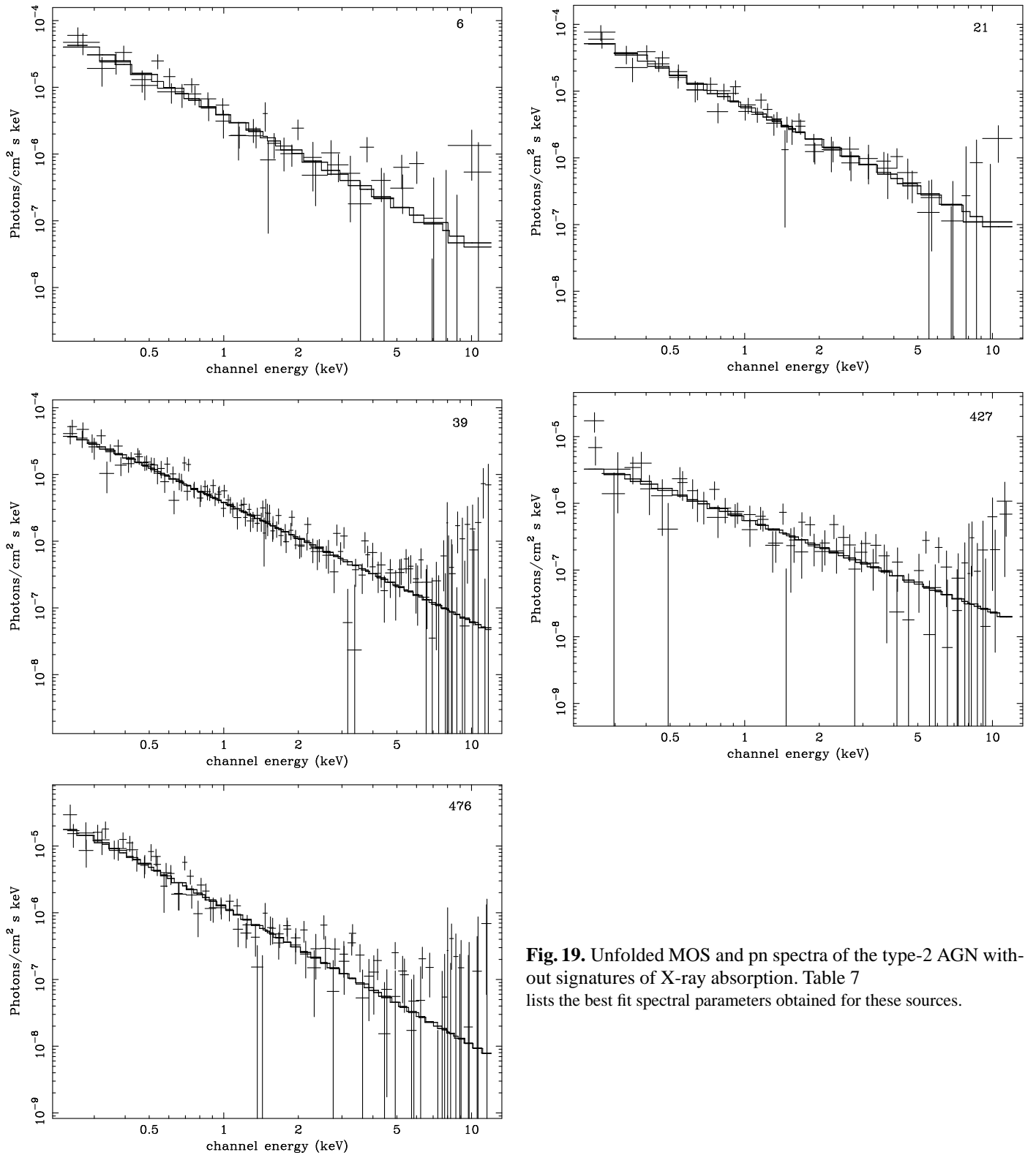


**Fig. 19.** Unfolded MOS and pn spectra of the type-2 AGN without signatures of X-ray absorption. Table 7 lists the best fit spectral parameters obtained for these sources.

XRB is significantly flatter than the typical spectrum of AGN. A population of heavily absorbed AGN, predicted by synthesis models of the XRB (e.g. Setti & Woltjer, 1989; Comastri et al.,

1995; Gilli et al., 2001; Gandhi & Fabian, 2003; Ueda et al., 2003), might account for this discrepancy.

We have carried out a stacking of MOS/pn time averaged spectra of the sources that we have analysed. Details on the

**Table 7.** X-ray properties of the type-2 AGN for which we did not found absorption in their X-ray spectrum.

ID	redshift	$\Gamma$	$N_{\text{H}}^{\text{intr}}$ (90% prob.)	$L_{2-10}$ erg s $^{-1}$	Equivalent width (eV)
(1)	(2)	(3)	(4)	(5)	(6)
6	0.528	$1.94 \pm 0.20$	$\leq 20.91$	43.07	576
21	0.498	$1.77 \pm 0.14$	$\leq 20.62$	43.28	1462
39	0.711	$1.79 \pm 0.08$	$\leq 20.66$	43.44	292
427	0.696	$1.40 \pm 0.20$	$\leq 21.08$	42.79	249
476	0.607	$2.07 \pm 0.17$	$\leq 20.22$	42.66	1393

Columns are as follows: (1) Source X-ray identification number; (2) redshift; (3)  $\Gamma$  from best fit model (for all sources the best fit model was a single power law); (4) upper limit in intrinsic (rest-frame) X-ray absorption (90% confidence); (5) logarithm of the 2-10 keV luminosity; (6) rest-frame equivalent width of an emission line centred at 6.4 keV with  $\sigma=0$  (the value of the EW was obtained using a Gaussian to fit the emission line)

analysis are given in Appendix A. The goal of this analysis was to compare the integrated emission of our sources, with an average spectral shape of  $\sim 1.92$  (see Sec. 9.1), with the spectrum of the XRB in the 2-7 keV energy band.

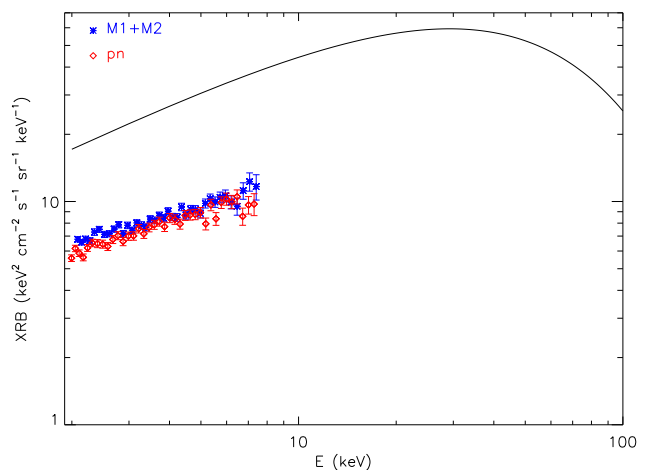
We fitted MOS and pn stacked spectra with *xspec* using a simple power law model. Then we divided the measured XRB intensities (in units of  $\text{keV}^2 \text{keV}^{-1} \text{cm}^{-2} \text{s}^{-1}$  at 1 keV) by the total solid angle covered by *XMM-Newton* ( $0.4 \text{ deg}^2$  or  $1.2185 \times 10^{-4} \text{ sr}$ ) to obtain the resolved fraction of XRB in the area surveyed.

Fig. 20 shows the total extragalactic XRB spectrum as measured by the HEAO-1 mission (solid line) but renormalised to the 2-8 keV intensity observed by De Luca & Molendi (2004). The points show the 2-10 keV XRB spectrum seen by MOS (diamonds) and pn (stars).

We found that the 2-7 keV XRB resolved by our sources was best fitted with a power law of  $\Gamma = 1.59 \pm 0.03$  and  $N=4.78 \pm 0.15 \text{ keV}^2 \text{keV}^{-1} \text{cm}^{-2} \text{s}^{-1} \text{sr}^{-1}$  (at 1 keV) for MOS data and  $\Gamma = 1.54 \pm 0.04$  and  $N=4.38 \pm 0.14 \text{ keV}^2 \text{keV}^{-1} \text{cm}^{-2} \text{s}^{-1} \text{sr}^{-1}$  (at 1 keV) for pn data. The integrated contribution of our sources is indeed harder than the spectrum of the brightest AGN, but still softer than the XRB at these energies. Since our sources have been selected in the 0.2-12 keV band, we probably missed faint absorbed sources. Worsley et al. (2004) did include fainter sources than the present study, and hence they reached a significantly higher integrated emission at 1 keV ( $N = 11 \pm 0.5 \text{ keV}^2 \text{keV}^{-1} \text{cm}^{-2} \text{s}^{-1} \text{sr}^{-1}$ ). A further component not detectable by *XMM-Newton* arising above 5 keV might also be present, as argued by Worsley et al. (2004).

### 13. Discussion and Conclusions

We have carried out a detailed study of the X-ray spectra of a sample of 123 objects detected with *XMM-Newton* in a deep observation in the *Lockman Hole* field. The EPIC spec-



**Fig. 20.** Spectrum of the extragalactic X-ray background as measured by the HEAO satellite but renormalised to the 2-8 keV intensity observed by De Luca & Mondeli (2004) (solid line). The points show the 2-7 keV stacked spectra of the sources that we have analysed (M1+M2 (diamonds) and pn (stars)).

tra of these sources have all more than 500 background subtracted counts (MOS+pn) in the energy interval from 0.2-12 keV. Thanks to the good signal to noise of the data we could study in detail the different spectral components that contribute to the X-ray emission of AGN in the above energy interval.

#### 13.1. X-ray continuum shape and intrinsic absorption

The 0.2-12 keV spectra of many AGN cannot be well reproduced with a single power law model. We found that this model is the best fit model for only  $\sim 53\%$  of the sample. The average continuum shape of our sources appears to harden at fainter 0.5-2 keV fluxes (see e.g. Giacconi et al., 2001; Mainieri et al., 2002; Mateos et al., 2005), but there are some indications that the same effect is seen for objects detected in the 2-10 keV band (Tozzi et al., 2001; Streblyanska et al., 2004). Two hypothesis have been suggested to explain it: X-ray absorption is more important at fainter fluxes or there exists a population of faint sources with intrinsically flatter continuum.

We confirm that this apparent effect is due to absorption. Both because it is not seen in the 2-10 keV band, and because it disappears when absorption is taken into account. We do not see any evidence for a population of intrinsically harder sources at faint fluxes. However, if sources with larger column densities were found, then we should see the hardening of  $\langle \Gamma \rangle$  in the 2-10 keV band. Using a single power law model, X-ray absorbed sources had the faintest 0.5-2 keV fluxes, but they had the same distribution of 2-10 keV fluxes than unabsorbed sources. Because of this, the average  $\Gamma$  obtained using a single power law model as a function of the 2-10 keV flux was measured to be harder ( $\Gamma \sim 1.7$ ) than the typical value of  $\sim 1.9$  found in unabsorbed AGN.

In the hard band we found no dependence of X-ray absorption or fraction of absorbed sources with flux. If observed (not

corrected for absorption) 0.5-2 keV fluxes are used, then the column density and the fraction of absorbed sources increase significantly at fainter fluxes. However, using unabsorbed 0.5-2 keV fluxes (i.e. fluxes corrected for the effect of absorption) the correlations are not observed and we obtain the same results than in the 2-10 keV band. Therefore to study the dependence of  $\Gamma$  with the X-ray flux it is important to first correct the fluxes for the effect of X-ray absorption. Another interesting result from our analysis is that allowing the objects to be X-ray absorbed we found a value of  $\langle\Gamma\rangle \sim 1.9$  at all 0.5-2 keV and 2-10 keV fluxes but with significant scatter in the points.

We have carried out a detailed study of the X-ray spectra of each individual object. We have searched for soft excess emission and for signatures of reflection at high energies (Compton reflection). We also studied the presence of Fe  $K\alpha$  emission. Using for each source the value of  $\Gamma$  obtained after including all these components to the fitting model we found that the scatter in  $\langle\Gamma\rangle$  is much smaller, and therefore is mostly due to the presence of other spectral components in the X-ray emission.

However we still expect some intrinsic scatter in  $\Gamma$ . To calculate the intrinsic dispersion in the continuum shape of our objects, we assumed that the distribution of  $\Gamma$  could be well represented with a Gaussian. Under this hypothesis, we found our sources to have an average spectral slope of  $\sim 1.92$  with an intrinsic dispersion of  $\sim 0.28$ .

### 13.2. Soft excess emission

Soft excess was detected in the time averaged spectra of 18 sources. However only in 9 objects (4 type-1 AGN, 4 type-2 AGN and 1 unidentified source) we could fit the spectral signatures with a black body model (a Raymond Smith gave an equally good fit). We found the average temperature of the black body to be  $0.09 \pm 0.01$  keV for type-1 AGN and  $0.26 \pm 0.08$  keV for type-2 AGN. The average 0.5-2 keV luminosities of the black body were found to be (in log units)  $43.42 \pm 0.43$  erg s<sup>-1</sup> in type-1 AGN and  $44.11 \pm 0.44$  erg s<sup>-1</sup> in type-2 AGN. The 0.5-2 keV luminosities of the soft excess component do not differ significantly between type-1 and type-2 AGN, but our results seem to indicate that the black body temperatures are slightly higher in type-2 AGN than in type-1 AGN. This might be due to a higher contribution from scattering in type-2 AGN. However due to the small number of AGN with soft excess analysed we can not reach any conclusion. The temperatures of the black body are in most cases  $\geq 60$  eV, and therefore the origin of the soft excess component in these sources cannot be explained as thermal emission from the accretion disc only. Comptonization of cool disc photons by hot electrons surrounding the accretion disc might be an alternative explanation.

In 9 sources (including 1 type-1 AGN, 3 type-2 AGN and 5 sources unidentified) the black body model could not fit the spectral signatures of the soft excess emission. For these sources we obtained a good fit with a scattering or partial covering model (two power laws with the same spectral index but different absorptions). The average covering fraction of the absorber was found to be  $0.82 \pm 0.06$ , which means that the scattering fraction in these sources is rather large ( $18 \pm 6\%$ ).

### 13.3. Reprocessed components

We found one object in our sample with a flattening in the spectral slope at high energies. The source is still unidentified so we used a model with two power laws to fit its X-ray emission.

Signatures of an emission line at high energies were found (F-test significance  $\geq 95\%$ ) in 8 sources (1 type-1 AGN, 5 type-2 AGN and 2 unidentified sources). Although in some sources the profiles of the lines did not appear to be symmetrical, the signal to noise of the spectra was not high enough to use more physical models. Therefore we fitted the lines in all the sources with a Gaussian model. For most AGN we found the centroids of the lines to be consistent (within the error bars) with being Fe  $K\alpha$  at an energy of  $\sim 6.4$  keV (rest frame). Only in one object we found the line centroid to be slightly higher than the expected value for neutral iron. In this source the line might arise as reflection in an ionised accretion disc.

In two objects we found significant widths for the emission lines. In another two sources the centroids of the lines were found at energies lower than 6.4 keV. In all these sources the emission lines might have relativistic line profiles, and therefore they might have been emitted in the inner regions of the black hole accretion disc.

### 13.4. X-ray spectra of AGN

We found the best fit average spectral slope to be  $1.89 \pm 0.03$  in type-1 AGN and  $1.71 \pm 0.03$  in type-2 AGN. These values seem to indicate that type-2 AGN have harder spectral slopes than type-1 AGN. However assuming that the values of  $\Gamma$  that we have obtained for each individual object follow a Gaussian distribution, and allowing the spectral slope to have intrinsic dispersion, the significance of type-2 AGN being harder than type-1 AGN is of  $1.62\sigma$ . This small difference in  $\langle\Gamma\rangle$  for type-1 and type-2 AGN might be due to the fact that if the signatures of absorption are not very significant, the detected values of  $N_{\text{H}}$  will tend to be lower than the real ones and then, the fitted  $\Gamma$  will be flatter. This effect will be more important for type-2 AGN where we expect more sources to be absorbed.

X-ray absorbed objects were found among type-1 AGN ( $\sim 10\%$ ) and type-2 AGN ( $\sim 77\%$ ). We found the fraction of absorbed objects in type-1 and type-2 AGN to be different with a significance of  $> 99.99\%$ . The distribution of absorbing column densities also suggest that type-1 AGN are less absorbed than type-2 AGN. A comparison with a KS test gave a significance of these distributions being different at 92% confidence.

We did not see a dependence of the AGN continuum shape with the X-ray luminosity or redshift. We found the same results for the column density.

### 13.5. Unabsorbed type-2 AGN

We studied in more detail the X-ray emission of the 5 type-2 AGN with unabsorbed MOS and pn X-ray spectra. All these sources have spectra with enough signal to noise, hence we should have been able to detect signatures of X-ray absorption if they are present. We have calculated the upper limit (90%) in the column density. We found that in all cases the values for the

column density are significantly lower than the typical values found in the absorbed type-2 AGN. If there is X-ray absorption in these sources, the low values of the column densities that we find could be explained as arising from the host galaxy. We argue that spectral variability is unlikely to be at the heart of the apparent X-ray/optical mismatch.

Finally we do not find compelling evidence that these sources are Compton-thick, although the [OIII] flux needs to be measured to reach a firm conclusion.

Table 8: Source X-ray properties

ID	<i>ROSAT</i>	RA	Dec	Class	<i>z</i>	Model	$\Gamma$	$\log(N_{\text{H}})$	$S_{0.5-2}$	$S_{2-10}$	$\log(L_{0.5-2})$	$\log(L_{2-10})$
(1)	(2)	(3)	(4)	(5)	(6)	(7)	(8)	(9)	(10)	(11)	(12)	(13)
607	-	10 53 01.86	+57 15 00.69	-	-	SPL	$1.21^{0.13}_{0.13}$		0.73	2.81		
599	54A	10 53 07.46	+57 15 05.84	AGNI	2.416	SPL	$1.46^{0.11}_{0.11}$		1.02	2.68	44.36	44.80
400	13A	10 52 13.29	+57 32 25.58	AGNI	1.873	SPL	$1.90^{0.06}_{0.06}$		0.63	0.84	44.14	44.27
63	-	10 52 36.49	+57 16 04.07	-	-	APL	$2.13^{0.32}_{0.23}$	$20.88^{0.24}_{0.38}$	0.54	0.66		
5	52A	10 52 43.30	+57 15 45.95	AGNI	2.144	SPL	$1.90^{0.06}_{0.06}$		1.60	2.16	44.68	44.68
6	504(51D)	10 51 14.30	+57 16 16.88	AGNII	0.528	SPL	$1.94^{0.20}_{0.19}$		0.87	1.11	42.97	43.07
16	-	10 51 46.64	+57 17 16.02	-	-	APL	$2.27^{2.08}_{0.98}$	$21.59^{0.40}_{0.24}$	0.22	0.44		
21	48B	10 50 45.67	+57 17 32.60	AGNII	0.498	SPL	$1.77^{0.14}_{0.14}$		1.34	2.18	43.07	43.28
26	-	10 52 32.99	+57 17 50.96	-	-	SPL	$1.09^{0.20}_{0.20}$		0.21	0.95		
31	-	10 52 00.34	+57 18 08.24	-	-	CAPL	$2.34^{0.30}_{0.63}$	$22.29^{0.12}_{0.16}$	0.15	0.99		
41	46A	10 51 19.14	+57 18 34.09	AGNI	1.640	APL	$2.06^{0.38}_{0.27}$	$21.82^{0.25}_{0.38}$	0.53	0.68	44.09	44.11
39	45Z	10 53 19.09	+57 18 53.58	AGNII	0.711	SPL	$1.79^{0.08}_{0.08}$		0.86	1.37	43.24	43.44
53	43A	10 51 04.39	+57 19 23.90	AGNI	1.750	APL	$1.83^{0.22}_{0.18}$	$21.68^{0.24}_{0.44}$	0.84	1.43	44.22	44.40
65	-	10 52 55.46	+57 19 52.80	-	-	APL	$1.57^{0.27}_{0.22}$	$21.24^{0.15}_{0.26}$	0.25	0.86		
74	905A	10 52 51.13	+57 20 15.70	-	-	SPL	$1.67^{0.21}_{0.20}$		0.19	0.35		
72	84Z	10 52 16.94	+57 20 19.71	AGNII	2.710*	APL	$1.69^{0.08}_{0.10}$	$23.28^{0.06}_{0.05}$	0.85	4.67	45.04	45.31
85	38A	10 53 29.50	+57 21 06.22	AGNI	1.145	SPL	$2.13^{0.09}_{0.08}$		0.72	0.69	43.77	43.74
86	-	10 53 09.68	+57 20 59.58	AGNI	3.420	SPL	$1.66^{0.17}_{0.16}$		0.23	0.45	44.16	44.45
88	39B	10 52 09.37	+57 21 05.43	AGNI	3.279	SPL	$1.73^{0.12}_{0.12}$		0.40	0.70	44.41	44.65
90	37A	10 52 48.09	+57 21 17.43	AGNI	0.467	SPL+SE	$2.10^{0.13}_{0.10}$		1.56	1.40	43.21	43.08
96	814(37G)	10 52 44.87	+57 21 24.84	AGNI	2.832	SPL	$2.08^{0.09}_{0.08}$		0.58	0.60	44.64	44.65
107	-	10 52 19.49	+57 22 15.26	AGNII	0.075	APL	$2.02^{0.23}_{0.28}$	$21.34^{0.09}_{0.21}$	0.26	0.48	40.78	40.83
120	-	10 52 25.17	+57 23 07.02	-	-	SPL	$1.91^{0.07}_{0.07}$		0.62	0.83		
108	-	10 50 50.91	+57 22 15.65	-	-	2SPL	$1.56^{0.18}_{0.18}$		0.78	8.48		
900	-	10 54 59.43	+57 22 18.84	-	-	APL	$1.72^{0.15}_{0.16}$	$21.03^{0.14}_{0.27}$	2.46	5.83		
121	434B	10 52 58.08	+57 22 51.95	AGNII	0.772	APL	$1.95^{0.25}_{0.20}$	$21.55^{0.16}_{0.24}$	0.31	0.52	43.05	43.15
135	513(34O)	10 52 54.39	+57 23 43.89	AGNI	0.761	SPL	$1.78^{0.04}_{0.04}$		1.56	2.50	43.56	43.77
124	634A	10 53 11.72	+57 23 09.07	AGNI	1.544	SPL	$1.69^{0.11}_{0.10}$		0.35	0.64	43.60	43.86
125	607(36Z)	10 52 19.90	+57 23 07.92	-	-	SPL	$1.66^{0.16}_{0.16}$		0.21	0.41		
142	-	10 52 03.74	+57 23 39.62	-	-	SPL	$1.81^{0.22}_{0.21}$		0.16	0.24		
133	35A	10 50 38.77	+57 23 39.67	AGNI	1.439	SPL	$2.04^{0.10}_{0.10}$		2.49	2.75	44.52	44.56
148	32A	10 52 39.66	+57 24 32.83	AGNI	1.113	SPL+SE	$2.12^{0.03}_{0.03}$		7.72	7.45	44.93	44.74

ID	ROSAT	RA	Dec	Class	$z$	Model	$\Gamma$	$\log(N_{\text{H}})$	$S_{0.5-2}$	$S_{2-10}$	$\log(L_{0.5-2})$	$\log(L_{2-10})$
(1)	(2)	(3)	(4)	(5)	(6)	(7)	(8)	(9)	(10)	(11)	(12)	(13)
166	-	10 52 31.98	+57 24 30.82	-	-	APL	$1.44^{0.19}_{0.24}$	$22.19^{0.14}_{0.16}$	0.09	1.48		
156	-	10 51 54.59	+57 24 09.28	AGNII**	2.365	APL	$2.40^{0.57}_{0.45}$	$22.65^{0.20}_{0.25}$	0.22	0.27	44.49	44.29
163	33A	10 51 59.88	+57 24 26.31	AGNI	0.974	APL	$1.52^{0.32}_{0.22}$	$21.57^{0.25}_{0.49}$	0.22	0.63	42.97	43.35
168	31A	10 53 31.72	+57 24 56.19	AGNI	1.956	SPL	$1.93^{0.03}_{0.03}$		3.30	4.22	44.92	45.03
172	-	10 53 15.71	+57 24 50.84	AGNII	1.17	APL	$2.26^{0.63}_{0.40}$	$23.22^{0.17}_{0.18}$	0.08	0.83	44.11	44.00
183	82A	10 53 12.27	+57 25 08.28	AGNI	0.96	SPL	$1.88^{0.07}_{0.07}$		0.57	0.78	43.39	43.53
176	30A	10 52 57.25	+57 25 08.77	AGNI	1.527	SPL	$2.21^{0.05}_{0.05}$		1.08	0.92	44.29	44.22
179	-	10 52 31.64	+57 25 03.93	-	-	CAPL	$2.07^{0.26}_{0.52}$	$22.42^{0.14}_{0.22}$	0.06	0.56		
174	-	10 51 20.63	+57 24 58.24	-	-	SPL	$1.37^{0.14}_{0.14}$		0.30	0.90		
186	-	10 51 49.93	+57 25 25.13	AGNII	0.676	APL	$1.70^{0.11}_{0.12}$	$22.21^{0.08}_{0.07}$	0.54	2.44	43.38	43.64
171	28B	10 54 21.22	+57 25 45.40	AGNII	0.205	APL	$1.73^{0.02}_{0.03}$	$21.33^{0.02}_{0.02}$	33.50	84.89	43.75	44.00
200	-	10 53 46.81	+57 26 07.77	-	-	APL	$2.37^{0.36}_{0.26}$	$20.93^{0.24}_{0.32}$	0.32	0.28		
187	-	10 50 47.96	+57 25 22.71	-	-	SPL	$1.98^{0.08}_{0.08}$		1.15	1.38		
191	29A	10 53 35.03	+57 25 44.13	AGNI	0.784	SPL	$1.82^{0.02}_{0.02}$		4.20	6.35	44.04	44.22
199	-	10 52 25.28	+57 25 51.27	-	-	APL	$1.80^{0.28}_{0.21}$	$21.99^{0.14}_{0.14}$	0.16	1.14		
217	-	10 51 11.60	+57 26 36.67	-	-	APL	$1.87^{0.11}_{0.12}$	$20.80^{0.17}_{0.31}$	0.65	1.10		
214	-	10 53 15.09	+57 26 30.65	-	-	APL	$1.88^{0.18}_{0.19}$	$21.41^{0.09}_{0.13}$	0.24	0.63		
222	-	10 53 51.67	+57 27 03.64	AGNII	0.917	APL	$1.88^{0.09}_{0.10}$	$21.45^{0.09}_{0.12}$	1.04	1.76	43.69	43.84
2020	27A	10 53 50.19	+57 27 11.61	AGNI	1.720	SPL	$2.23^{0.07}_{0.07}$		0.97	0.80	44.39	44.30
226	-	10 51 20.49	+57 27 03.47	-	-	SPL	$1.88^{0.10}_{0.10}$		0.50	0.70		
243	-	10 51 28.14	+57 27 41.55	-	-	CAPL	$1.82^{0.19}_{0.17}$	$22.02^{0.08}_{0.08}$	0.51	3.49		
254	486A	10 52 43.37	+57 28 01.49	AGNII	1.210	APL	$1.76^{0.13}_{0.13}$	$22.18^{0.08}_{0.10}$	0.32	0.91	43.59	43.81
261	80A	10 51 44.63	+57 28 08.89	AGNI	3.409	SPL	$1.63^{0.08}_{0.08}$		0.45	0.92	44.44	44.74
259	-	10 53 05.60	+57 28 12.50	AGNII	0.792	APL+SE	$1.22^{0.14}_{0.18}$	$23.24^{0.12}_{0.13}$	0.07	3.39	43.32	43.90
270	120A	10 53 09.28	+57 28 22.65	AGNI	1.568	SPL+SE	$2.17^{0.06}_{0.09}$		0.80	0.72	44.32	44.12
267	428E	10 53 24.54	+57 28 20.65	AGNI	1.518	APL	$1.74^{0.10}_{0.10}$	$21.27^{0.12}_{0.40}$	0.53	0.97	43.81	44.05
287	821A	10 53 22.04	+57 28 52.76	AGNI	2.300	SPL	$1.67^{0.14}_{0.13}$		0.20	0.39	43.74	44.02
268	-	10 53 48.09	+57 28 17.75	-	-	APL	$1.83^{0.19}_{0.20}$	$21.81^{0.13}_{0.11}$	0.24	1.21		
277	25A	10 53 44.85	+57 28 42.24	AGNI	1.816	SPL	$1.74^{0.04}_{0.04}$		1.18	2.03	44.31	44.55
272	26A	10 50 19.40	+57 28 13.99	AGNII	0.616	APL	$2.39^{0.17}_{0.17}$	$21.58^{0.10}_{0.13}$	1.39	1.38	43.62	43.43
290	901A	10 52 52.74	+57 29 00.81	AGNII	0.204	APL+SE	$1.86^{0.39}_{0.22}$	$23.60^{0.07}_{0.14}$	0.14	1.79	42.69	42.83
369	-	10 51 06.50	+57 15 31.92	-	-	SPL	$1.96^{0.11}_{0.11}$		1.99	2.46		
300	426A	10 53 03.64	+57 29 25.56	AGNI	0.788	CAPL	$1.98^{0.18}_{0.15}$	$22.09^{0.16}_{0.22}$	0.50	0.87	43.32	43.40
306	-	10 52 06.84	+57 29 25.43	AGNII	0.708	APL	$1.38^{0.24}_{0.20}$	$22.20^{0.17}_{0.17}$	0.16	1.03	42.76	43.23

ID	ROSAT	RA	Dec	Class	$z$	Model	$\Gamma$	$\log(N_{\text{H}})$	$S_{0.5-2}$	$S_{2-10}$	$\log(L_{0.5-2})$	$\log(L_{2-10})$
(1)	(2)	(3)	(4)	(5)	(6)	(7)	(8)	(9)	(10)	(11)	(12)	(13)
321	23A	10 52 24.74	+57 30 11.40	AGNI	1.009	SPL	$1.70^{0.08}_{0.08}$		0.39	0.71	43.22	43.48
326	117Q	10 53 48.80	+57 30 36.09	AGNII	0.78	APL	$1.53^{0.06}_{0.05}$	$21.96^{0.06}_{0.06}$	1.38	5.49	43.71	44.08
350	-	10 52 41.65	+57 30 39.97	-	-	SPL	$1.28^{0.14}_{0.14}$		0.14	0.50		
332	77A	10 52 59.16	+57 30 31.81	AGNI	1.676	SPL	$1.62^{0.04}_{0.04}$		1.08	2.22	44.14	44.45
411	53A	10 52 06.02	+57 15 26.41	AGNII	0.245	CAPL	$1.63^{0.22}_{0.19}$	$22.18^{0.13}_{0.16}$	0.85	4.84	42.63	42.94
2024	-	10 54 10.68	+57 30 56.73	-	-	SPL	$2.02^{0.07}_{0.07}$		0.82	0.93		
343	-	10 50 41.22	+57 30 23.31	-	-	SPL	$1.54^{0.19}_{0.18}$		0.44	1.01		
342	16A	10 53 39.62	+57 31 04.89	AGNI	0.586	SPL+SE	$2.26^{0.04}_{0.05}$		4.84	3.81	43.92	43.78
351	-	10 51 46.39	+57 30 38.14	-	-	SPL	$1.87^{0.15}_{0.14}$		0.21	0.30		
353	19B	10 51 37.27	+57 30 44.43	AGNI	0.894	SPL	$1.72^{0.10}_{0.10}$		0.40	0.71	43.12	43.37
354	75A	10 51 25.25	+57 30 52.33	AGNI	3.409	SPL	$1.75^{0.08}_{0.07}$		0.71	1.20	44.71	44.94
358	17A	10 51 03.86	+57 30 56.65	AGNI	2.742	SPL	$1.78^{0.08}_{0.07}$		1.13	1.83	44.72	44.93
355	-	10 52 37.33	+57 31 06.67	AGNII	0.708	APL	$1.60^{0.12}_{0.12}$	$21.17^{0.17}_{0.28}$	0.36	0.86	42.87	43.19
385	14Z	10 52 42.37	+57 32 00.64	AGNII	1.380	APL	$1.83^{0.08}_{0.08}$	$22.33^{0.04}_{0.04}$	0.76	2.10	44.16	44.33
364	18Z	10 52 28.36	+57 31 06.57	AGNI	0.931	SPL	$1.79^{0.13}_{0.13}$		0.23	0.37	42.94	43.14
901	-	10 50 05.55	+57 31 09.01	-	-	SPL	$1.64^{0.14}_{0.12}$		0.79	1.58		
902	73C	10 50 09.12	+57 31 46.29	AGNI	1.561	SPL	$1.50^{0.14}_{0.14}$		0.78	1.94	43.88	44.28
377	-	10 52 52.11	+57 31 38.02	-	-	APL	$1.81^{0.21}_{0.21}$	$21.87^{0.11}_{0.12}$	0.17	0.92		
384	-	10 53 21.63	+57 31 49.44	-	-	APL	$2.22^{0.19}_{0.26}$	$21.33^{0.11}_{0.17}$	0.26	0.40		
387	15A	10 52 59.78	+57 31 56.69	AGNI	1.447	SPL	$2.27^{0.11}_{0.11}$		0.37	0.28	43.78	43.67
394	-	10 52 51.40	+57 32 02.03	AGNII	0.664	APL	$1.85^{0.22}_{0.22}$	$21.24^{0.24}_{0.45}$	0.17	0.29	42.55	42.71
406	828A	10 53 57.16	+57 32 44.00	AGNI	1.282	SPL	$2.12^{0.10}_{0.10}$		0.62	0.60	43.82	43.80
419	-	10 54 00.46	+57 33 22.19	-	-	APL	$1.81^{0.23}_{0.17}$	$21.62^{0.12}_{0.11}$	0.41	1.54		
407	12A	10 51 48.69	+57 32 50.07	AGNII	0.990	CAPL	$1.25^{0.10}_{0.10}$	$22.69^{0.12}_{0.11}$	0.57	4.89	43.64	44.20
424	-	10 52 37.93	+57 33 22.65	AGNII	0.707	APL+SE	$1.70^{0.32}_{0.18}$	$22.95^{0.12}_{0.12}$	0.22	2.36	43.50	43.74
427	-	10 52 27.88	+57 33 30.65	AGNII	0.696	SPL	$1.40^{0.20}_{0.20}$		0.14	0.39	42.33	42.79
430	11A	10 51 08.19	+57 33 47.06	AGNI	1.540	APL	$1.42^{0.08}_{0.08}$	$21.58^{0.13}_{0.19}$	1.24	3.83	44.09	44.53
458	-	10 51 06.22	+57 34 36.67	-	-	CAPL	$1.34^{0.39}_{0.16}$	$22.31^{0.16}_{0.20}$	0.28	4.43		
442	805A	10 53 47.28	+57 33 50.41	AGNI	2.586	SPL	$1.76^{0.15}_{0.14}$		0.33	0.55	44.12	44.34
443	-	10 52 36.89	+57 33 59.80	AGNII	1.877	APL	$2.05^{0.42}_{0.34}$	$23.22^{0.16}_{0.18}$	0.17	0.97	44.42	44.46
474	-	10 51 28.13	+57 35 04.20	-	-	SPL	$1.98^{0.11}_{0.11}$		0.47	0.56		
451	-	10 52 07.87	+57 34 17.48	-	-	APL	$1.94^{0.18}_{0.21}$	$21.31^{0.11}_{0.15}$	0.29	0.62		
450	477A	10 53 05.98	+57 34 26.70	AGNI	2.949	SPL	$2.03^{0.10}_{0.10}$		0.44	0.49	44.53	44.57
453	804A	10 53 12.24	+57 34 27.39	AGNI	1.213	SPL	$2.05^{0.14}_{0.14}$		0.31	0.34	43.44	43.47



ID	ROSAT	RA	Dec	Class	$z$	Model	$\Gamma$	$\log(N_{\text{H}})$	$S_{0.5-2}$	$S_{2-10}$	$\log(L_{0.5-2})$	$\log(L_{2-10})$
(1)	(2)	(3)	(4)	(5)	(6)	(7)	(8)	(9)	(10)	(11)	(12)	(13)
456	9A	10 51 54.30	+57 34 38.66	AGNI	0.877	SPL	$2.01^{0.05}_{0.05}$		1.25	1.44	43.68	43.74
491	-	10 51 41.91	+57 35 56.00	-	-	APL	$2.18^{0.23}_{0.25}$	$21.24^{0.15}_{0.25}$	0.33	0.48		
469	-	10 54 07.21	+57 35 24.89	-	-	SPL	$2.14^{0.04}_{0.04}$		3.86	3.62		
475	6A	10 53 16.51	+57 35 52.23	AGNI	1.204	SPL	$1.78^{0.02}_{0.02}$		10.21	16.61	44.85	45.06
476	827A	10 53 03.43	+57 35 30.80	AGNII	0.607	SPL	$2.07^{0.17}_{0.17}$		0.27	0.29	42.64	42.66
505	104A	10 52 41.54	+57 36 52.85	AGNII	0.137	CAPL	$1.72^{0.09}_{0.08}$	$21.69^{0.11}_{0.08}$	1.36	3.96	42.04	42.29
504	-	10 54 26.22	+57 36 49.05	-	-	APL+SE	$1.98^{0.19}_{0.10}$	$22.66^{0.06}_{0.06}$	1.01	42.52		
511	-	10 53 38.50	+57 36 55.47	AGNII	0.704	APL+SE	$2.62^{0.73}_{0.29}$	$22.81^{0.15}_{0.14}$	0.19	0.96	43.97	43.58
518	-	10 53 36.33	+57 37 32.14	-	-	APL	$2.38^{0.52}_{0.19}$	$21.09^{0.14}_{0.20}$	0.48	0.47		
523	-	10 51 29.98	+57 37 40.71	-	-	SPL	$1.94^{0.09}_{0.09}$		0.92	1.17		
529	-	10 51 37.30	+57 37 59.11	-	-	CAPL	$1.98^{0.20}_{0.21}$	$21.93^{0.23}_{0.20}$	1.51	2.88		
532	801A	10 52 45.36	+57 37 48.69	AGNI	1.677	SPL	$2.32^{0.21}_{0.20}$		0.22	0.16	43.74	43.60
527	5A	10 53 02.34	+57 37 58.62	AGNI	1.881	SPL	$1.91^{0.06}_{0.05}$		1.13	1.50	44.40	44.53
537	-	10 50 50.04	+57 38 21.79	-	-	SPL	$2.40^{0.08}_{0.08}$		3.04	1.95		
548	832A	10 52 07.53	+57 38 41.40	AGNI**	2.730	SPL	$1.79^{0.15}_{0.14}$		0.30	0.48	44.15	44.13
557	-	10 52 07.75	+57 39 07.49	-	-	APL	$2.01^{0.36}_{0.17}$	$20.94^{0.22}_{0.45}$	0.33	0.49		
553	2A	10 52 30.06	+57 39 16.81	AGNI	1.437	APL	$2.08^{0.04}_{0.04}$	$21.20^{0.12}_{0.14}$	2.87	3.14	44.62	44.64
555	-	10 51 52.07	+57 39 09.41	-	-	SPL	$1.84^{0.12}_{0.12}$		0.49	0.72		
594	-	10 52 48.40	+57 41 29.14	-	-	SPL	$1.59^{0.24}_{0.24}$		0.38	0.82		
2045	-	10 52 04.47	+57 41 15.65	-	-	SPL	$1.89^{0.09}_{0.09}$		0.94	1.28		
584	-	10 52 06.28	+57 41 25.53	-	-	SPL	$2.17^{0.07}_{0.08}$		1.61	1.45		
591	-	10 52 23.17	+57 41 24.62	-	-	SPL	$2.08^{0.14}_{0.14}$		0.59	0.61		
601	-	10 51 15.91	+57 42 08.59	-	-	SPL	$1.84^{0.20}_{0.19}$		1.30	1.92		

Columns are as follows: (1) XMM-Newton identification number; (2) ROSAT identification number; (3) Right ascension (J2000); (4) Declination (J2000); (5) Optical class from optical spectroscopy; (6) Source redshift; (7) Best fit model of the X-ray spectrum of each object: SPL: single power law, APL: absorbed power law, SE: Soft-excess emission, CAPL: absorption with partial covering absorber, 2SPL: two power laws; (8) Slope of the broad band continuum emission; (9) Logarithm of the hydrogen column density of the X-ray absorber (observed  $N_{\text{H}}$  if the source is still unidentified or rest-frame absorption if the source is identified; (10) and (11) 0.5-2 and 2-10 keV flux in units of  $10^{-14}$  erg  $\text{cm}^{-2}$   $\text{s}^{-1}$  obtained from the best fit model; (12) and (13) logarithm of the 0.5-2 and 2-10 keV luminosities (corrected for absorption) for the identified sources obtained from the best fit model.

The source coordinates RA and DEC, are not the X-ray positions from the *Lockman Hole* catalogue (H. Brunner et al. 2005, in preparation), but the centres of the regions used to extract the spectra of the objects.

\* Source photometric redshift.

\*\* BAL QSO

*Acknowledgements.* SM acknowledges support from a Universidad de Cantabria fellowship. XB, FJC and MTC acknowledge financial support from the Spanish Ministerio de Educación y Ciencia, under project ESP2003-00812. Some of the data presented here were obtained at the W. M. Keck Observatory, which is operated as a scientific partnership among the California Institute of Technology, the University of California, and the National Aeronautics and Space Administration. The Observatory was made possible by the generous financial support of the W. M. Keck Foundation. We also thank the anonymous referee for his/her suggestions that helped to improve the manuscript considerably.

## References

- Antonucci, R. 1993 ARA&A, 31, 473
- Awaki, H., Kunieda, H., Tawara, Y. & Koyama, K. 1991 PASJ, 43L, 37A
- Barcons X., Carrera F.J., & Ceballos, M. T. 2003 MNRAS, 346, 897
- Bassani, L., Dadina, M., Maiolino, R., Salvati, M. et al. 1999 ApJS, 121, 473
- Bevington, P.R., Robinson, D.K., 1992 Data reduction and error analysis for the Physical sciences, McGraw Hill
- Brusa, M., Comastri, A., Mignoli, M., et al. 2003, A&A, 409, 65
- Caccianiga, A., Severgnini, P., Braito, V., et al. 2004, A&A, 416, 901
- Carrera, F.J., Page M.J., & Mittaz J.P.D. 2004, A&A, 420, 163
- Della Ceca, R., Maccacaro, T., Caccianiga, A., Severgnini, P., et al. 2004 A&A, 428, 383
- Comastri, A., Setti, G., Zamorani, G., et al. 1995, A&A, 296, 1
- Corral, A., Barcons, X., Carrera, F.J., Ceballos, M.T. & Mateos, S. 2005 A&A accepted, astro-ph/0410347
- De Luca, A. & Molendi, S. 2004 A&A, 419, 837
- F. Fiore F., Giommi P., Vignali C., et al. 2001, MNRAS, 327, 771
- Gandhi, P. & Fabian, A. C. 2003 MNRAS, 339, 1095
- Gabriel, C., Denby, M., Fyfe, D. J., et al. 2004 in Astronomical Data Analysis Software and Systems XIII, ed. F. Ochsenbein, M. Allen, & D. Egret, ASP Conf. Ser., 314, 759
- Georgantopoulos, I., Georgakakis, A., Akylas, A., Stewart, G.C., Giannakis, O., et al. 2004, MNRAS, 352, 91
- Giacconi, R., Rosati, P., Tozzi, P. et al. 2001, ApJ, 551, 624
- Gilli, R., Salvati, M. & Hasinger, G. 2001, A&A, 366, 407
- Hasinger, G., Altieri, B., Arnaud, M., et al. 2001, A&A, 365, L45
- Kirsh, M., 2004 'EPIC status of calibration and data analysis', XMM-Newton SOC, XMM-SOC-CAL-TN-0018
- Lehmann, I., Hasinger, G., Schmidt, M., et al. 2001, A&A, 371, 833
- Lockman, F.J., Jahoda, K., & McCammon, D. 1986, ApJ, 302, 432
- Maccacaro, T., Gioia L.M., Wolter A., et al. 1988, ApJ, 326, 680
- Mainieri, V., Bergeron, J., Hasinger, G., et al. 2002, A&A, 393, 425
- Mateos, S., Barcons, X., Carrera, F.J., et al. 2005, A&A, accepted, astro-ph/0412390
- Marshall, F. E., Boldt, E. A., Holt, S. S., Miller, R. B., et al. 1980 ApJ, 235, 4
- Mittaz, J.P.D., Carrera F. J., Romero-Colmenero E., et al. 1999, MNRAS, 308, 233
- Nandra, K. & Pounds, K.A. 1994, MNRAS, 268, 405
- Nandra, K., Pounds, K. A., Stewart, G. C. et al. 1991 MNRAS, 248, 760
- Page, M.J., Mittaz, J.P.D., & Carrera, F.J. 2001, MNRAS, 325, 575
- Page, M.J., McHardy, I.M., Gunn, K.F., et al. 2003, AN, 324, 101
- Panessa, F. & Bassani, L. 2002, A&A, 394, 435
- Pappa, A., Georgantopoulos, I., Stewart, G.C., et al. 2001, MNRAS, 326, 995
- Perola, G.C., Puccetti, S., Fiore, F., Sacchi, N., Brusa, M., et al. 2004, A&A (in press)
- Piconcelli, E., Cappi, M., Bassani, L. et al. 2002, A&A, 394, 835
- Piconcelli, E., Cappi, M., Bassani, L. et al. 2003, A&A
- Pounds, K. A., Nandra, K., Stewart, G. C., George, I. M. & Fabian, A. C., 1990 Nature, 344, 132
- Pounds, K. A., Nandra, K., Stewart, G. C. & Leighly, K. 1989 MNRAS, 240, 769
- Risaliti, G.; Maiolino, R. & Salvati, M. 1999, AJ, 522, 157
- Schartel N., Schmidt M., Fink H. H., Hasinger G. et al. 2001, A&A 320,696
- Schmidt, M., Hasinger, G., Gunn, J., et al. 1998, A&A, 329, 495
- Setti, G. & Woltjer, L. 1989, A&A, 224, L21
- Stevens, J. A., Page, M. J., Ivison, R. J., et al. 2005 MNRAS, submitted
- Streblyanska, A., Bergeron, J., Brunner, H., Finoguenov, A., et al. 2004 Nuclear Physics B (Proc. Suppl.) 132, 232
- Streblyanska, A., Hasinger, G., Finoguenov, A., Barcons, X., Mateos, S. & Fabian, A.C. 2005 A&A, 432, 395
- Tozzi, P., Bergeron, J., Borgani, S., Giacconi, R., et al. 2001 Proceedings of the XXI Moriond Astrophysics Meeting
- Tozzi, P., Rosati, P., Nonino, M., Bergeron, J., et al. 2001, AJ, 562, 42
- Ueda, Y., Akiyama, M., Ohta, K. & Miyaji, T. 2003, ApJ, 598, 886
- Worsley, M.A., Fabian, A.C., Barcons, X., Mateos, S., Hasinger, G., Brunner, H. 2004, MNRAS, 352, L28
- Worsley, M.A., Fabian, A.C., Bauer, F.E., Alexander, D.M. et al. 2005 MNRAS, accepted, astro-ph/0412266

## Appendix A: Stacking of spectra of *Lockman Hole* sources

To calculate the contribution to the Cosmic X-ray background from our sources, MOS and pn spectra have been stacked.

We have kept MOS and pn data separately because of the different instrumental responses and to provide support to the results. In addition, as it was explained in Sec. 6, MOS and pn time averaged spectra were not necessarily built using the same set of observations, hence the normalisations of the XRB spectrum obtained with MOS and pn might be slightly different.

At the time of this study there were calibration uncertainties between MOS and pn data at energies below  $\sim 1$  keV (pn gives higher fluxes below 0.7 keV by 10-15% with respect to MOS, see Kirsh et al. 2004). We also found our data to be rather uncertain at energies  $\geq 7$  keV. Because of the rapid decrease in the effective area of the X-ray detectors at energies  $\geq 5$  keV the signal to noise of the data becomes very low. In addition we know that the particle background is very important at high energies. Therefore we restricted our analysis to the 2-7 keV energy interval where we know that our results will not be affected by calibration problems or inaccurate background subtraction.

MOS and pn stacked spectra were obtained with the following procedure: suppose we want to add two spectra having exposure times  $\tau_1$  and  $\tau_2$ , backscalls  $b_1$  and  $b_2$  and response matrices  $rsp_1$  and  $rsp_2$ , and that the corresponding background extraction regions have exposure times  $tb_1$  and  $tb_2$  and backscalls  $bb_1$  and  $bb_2$ :

1. Add spectra: The total backscale will be  $b_1+b_2^{12}$  and the total exposure time  $(\tau_1 \times b_1 + \tau_2 \times b_2) / (b_1 + b_2)$ .

<sup>12</sup> Note that we want to extract the XRB from the regions where we have the sources, and therefore, we are accumulating counts in an increasing solid angle.

2. Add background files: The total backscale will be  $bb1+bb2$  and the total exposure time  $(tb1\times bb1+tb2\times bb2)/(bb1+bb2)$ .
3. Add response matrices. The combined response matrix will be  $(t1\times b1)\times rsp1+(t2\times b2)\times rsp2/(t1\times b1+t2\times b2)$ .

This procedure can be trivially extended to stack any number of sources.